USER GUIDE
Planetary-Code-Collection:
Thermal and Ice Evolution Models
for Planetary Surfaces

Norbert Schörghofer (norbert@psi.edu)
Honolulu, Hawaii

2002–2022
Last updated April 19, 2022

Contents

Preface

Companion to `https://github.com/nschorgh/Planetary-Code-Collection/`

Cite user guide or source code as:

N. Schörghofer. Planetary-Code-Collection: Thermal and Ice Evolution Models for Planetary Surfaces, 2022. GitHub. doi:10.5281/zenodo.594268 https://github.com/nschorgh/Planetary-Code-Collection/

The most recent release is usually behind the most recent version available on GitHub, but releases have DOIs that can be cited.

Releases are available from GitHub and Zendodo. Each release has a version number and a dedicated DOI, whereas the above DOI refers to all versions, past and future. Individual DOIs are listed at `https://zenodo.org/record/594268`

Technical Notes:
Most of the code was developed with a `gfortran` compiler on Intel processors. Many components were also run on various Linux clusters, sometimes using other compilers. The non-portable `real(8)` and `real*8` are meant to correspond to an 8-byte floating point number.

Part 1

1D Thermal Model for Planetary Surfaces

1-Dimensional Numerical Model of Thermal Conduction and Surface Energy Balance

The heat flow in the shallow subsurface is described by the heat equation:

$$\rho c \frac{\partial T}{\partial t} = \frac{\partial}{\partial z}\left(k\frac{\partial T}{\partial z}\right) \tag{1.1}$$

where T is temperature, t time, z depth, ρc the volumetric heat capacity, and k thermal conductivity.

The (negative of the) heat flux is $F = k\dfrac{\partial T}{\partial z}$.

Boundary conditions are specified below.

1.1   Semi-Implicit Scheme on Irregular Grid

Authors & History: originally implemented by Samar Khatiwala in 2001 (including upper radiation boundary condition for semi-implicit scheme); extended to variable thermal properties and irregular grid by Norbert Schörghofer 2002–2003; added predictor-corrector step in 2019

A flux-conservative discretization on an irregularly-spaced grid is given by

$$\frac{\partial}{\partial z}F_j = \frac{F_{j+\frac{1}{2}} - F_{j-\frac{1}{2}}}{(z_{j+1} - z_{j-1})/2} = 2\frac{k_{j+\frac{1}{2}}\frac{T_{j+1}-T_j}{z_{j+1}-z_j} - k_{j-\frac{1}{2}}\frac{T_j-T_{j-1}}{z_j-z_{j-1}}}{z_{j+1} - z_{j-1}}$$

Subscript j refers to position z_j. The spatial discretization of the heat equation (1.1) then becomes

$$(\rho c)_j \frac{\partial T_j}{\partial t} = \frac{2k_{j+\frac{1}{2}}}{(z_{j+1} - z_j)(z_{j+1} - z_{j-1})}T_{j+1} - \frac{2}{z_{j+1} - z_{j-1}}\left(\frac{k_{j+\frac{1}{2}}}{z_{j+1} - z_j} + \frac{k_{j-\frac{1}{2}}}{z_j - z_{j-1}}\right)T_j +$$

$$+ \frac{2k_{j-\frac{1}{2}}}{(z_j - z_{j-1})(z_{j+1} - z_{j-1})}T_{j-1}$$

4

introduce $\quad \alpha_j = \dfrac{\Delta t}{(\rho c)_j} \dfrac{k_{j+\frac{1}{2}}}{(z_{j+1} - z_j)(z_{j+1} - z_{j-1})} \quad$ and $\quad \gamma_j = \dfrac{\Delta t}{(\rho c)_j} \dfrac{k_{j-\frac{1}{2}}}{(z_j - z_{j-1})(z_{j+1} - z_{j-1})}$

$$(1.2)$$

$$\frac{\partial T_j}{\partial t} = 2\alpha_j T_{j+1} - 2(\alpha_j + \gamma_j)T_j + 2\gamma_j T_{j-1}$$

A semi-implicit time discretization of (1.1) is of the form (Crank and Nicolson, 1947; Press et al., 1992)

$$(\rho c)_j \frac{T_j^{n+1} - T_j^n}{\Delta t} = \frac{1}{2}\left(\frac{\partial}{\partial z}F_j^{n+1} + \frac{\partial}{\partial z}F_j^n\right)$$

where superscript n refers to the time step. Hence,

$$T_j^{n+1} - T_j^n = \alpha_j T_{j+1}^{n+1} - (\alpha_j + \gamma_j)T_j^{n+1} + \gamma_j T_{j-1}^{n+1} + \alpha_j T_{j+1}^n - (\alpha_j + \gamma_j)T_j^n + \gamma_j T_{j-1}^n$$

which leads to the system of equations

$$\boxed{-\alpha_j T_{j+1}^{n+1} + (1 + \alpha_j + \gamma_j)T_j^{n+1} - \gamma_j T_{j-1}^{n+1} = \alpha_j T_{j+1}^n + (1 - \alpha_j - \gamma_j)T_j^n + \gamma_j T_{j-1}^n} \quad 1 < j < N$$

$$(1.3)$$

This tridiagonal linear system can be solved in $O(N)$ steps.

Whereas the temperature T_j is defined on grid point z_j, the conductivity k is defined in between points. In the equations above, $(\rho c)_j$ is defined on z_j, but in the program implementations, $2(\rho c)_j = (\rho c)_{j+\frac{1}{2}} + (\rho c)_{j-\frac{1}{2}}$. In this way, the thermal properties k and ρc are defined on the same points. And they do not need to be defined at an interface of two layers with different thermal properties when that interface coincides with a grid point. Since array indices must be integers, we choose $\texttt{k[j]} = k_{j-\frac{1}{2}}$, and the same for ρc.

Although the derivation was made with time-constant thermal parameters k and ρc, it remains valid if these parameters change slowly with time.

1.1.1 Upper boundary condition: Stefan-Boltzmann radiation law

The surface energy balance is given by

$$Q + k\left.\frac{\partial T}{\partial z}\right|_{z=0} = \epsilon\sigma T^4\big|_{z=0} \tag{1.4}$$

Q is the incoming solar flux including any atmospheric contribution. On the right-hand side, ϵ is the (infrared) emissivity of the surface and σ is the Stefan-Boltzmann constant. To apply an implicit method, the nonlinear boundary condition needs to be linearized.

Introduce the auxiliary quantity T_0, such that surface temperature $T_s = (T_0 + T_1)/2$

$$\left.\frac{\partial T}{\partial z}\right|_{z=0} = \frac{T_1 - T_0}{\Delta z} \quad \text{and} \quad T^4\big|_{z=0} = \left(\frac{T_0 + T_1}{2}\right)^4 \quad \text{with} \quad \Delta z = 2z_1$$

$T = T_r + T' \qquad T_r$ is a reference temperature around which we linearize

$$
\begin{aligned}
Q + k_{1/2}\frac{T_1 - T_0}{\Delta z} &= \epsilon\sigma\left(\frac{2T_r + T_0' + T_1'}{2}\right)^4 \\
&\approx \epsilon\sigma T_r^4 + 2\epsilon\sigma T_r^3(T_0' + T_1') = -3\epsilon\sigma T_r^4 + 2\epsilon\sigma T_r^3(T_0 + T_1)
\end{aligned}
$$

$T_0 \left(\frac{k_{1/2}}{\Delta z} + B(T_r) \right) = Q + 3\epsilon\sigma T_r^4 + T_1 \left(\frac{k_{1/2}}{\Delta z} - B(T_r) \right)$ where $B(T_r) = 2\epsilon\sigma T_r^3$

Introduce $a = (Q + 3\epsilon\sigma T_r^4) / \left(\frac{k}{\Delta z} + B \right)$ and $b = \left(\frac{k_{1/2}}{\Delta z} - B \right) / \left(\frac{k_{1/2}}{\Delta z} + B \right)$.

The relation for $j = 1$ is then

$$-\alpha_1 T_2^{n+1} + (1 + \alpha_1 + \gamma_1 - \gamma_1 b^{n+1})T_1^{n+1} = \alpha_1 T_2^n + (1 - \alpha_1 - \gamma_1 + \gamma_1 b^n)T_1^n + \gamma_1(a^n + a^{n+1}) \quad (1.5)$$

Define $\beta = \frac{\Delta t}{(\rho c)_1} \frac{1}{2\Delta z^2}$, then $\alpha_1 = \beta k_{3/2}$ and $\gamma_1 = \beta k_{1/2}$. The surface temperature is computed as

$$T_s = \frac{1}{2}(T_0 + T_1) = \frac{1}{2}(a + bT_1 + T_1)$$

Choose $T_r^n = T_s^n$. The semi-implicit solver with this boundary condition is implemented in `conductionQ.f90`.

The uppermost layer is a half-layer, and the first few grid points must be chosen as $z_0 = 0$ and $z_2 = 3z_1$ (in other words $z_1 = \Delta z/2$, $z_2 = z_1 + \Delta z$). The coefficients for the nonlinear upper boundary condition are designed for that. Subroutine `setgrid` can be used to generate a suitable grid.

Modified treatment of the upper boundary helpful in some situations: The linearization of the Stefan-Boltzmann law, σT^4, works well as long as the surface temperature changes slowly. The above approximation works very well for most situations, such as Mars orbit and a horizontal surface. A temporary instability, where the surface temperature overshoots significantly, was encountered in two situations: i) A sloped, shadowed surface emerges into sunlight. In this case the energy input changes abruptly. ii) For asteroid orbits with high eccentricity and very small perihelion distances, when the pole emerges from winter into sunlight near perihelion. This transition is continuous, but the change in input energy is nevertheless dramatic.

Above, the thermal emission is linearized around the reference temperature $T_r^n = T_s^n$. If T_s^{n+1} is far from T_s^n, a significant error was incurred in the evaluation of the emitted energy. This can be addressed by repeating the calculation with a new reference temperature T_r somewhere in between T_s^n and T_s^{n+1}. An empirical choice is the geometric mean between the previous reference temperature and the new surface temperature. This method is essentially a predictor-corrector step, iteratively applied until T_r is within 20% of $T_s^{(n+1)}$.

Another approach is "artificial flux smoothing" where the time step is subdivided into many substeps, using linear interpolation of the incoming flux from Q^n to Q^{n+1}. It turns a discontinuous change in Q into a continuous change. However, this approach does not identify a nascent instability or answer how many substeps are required to cure it.

1.1.2   Upper boundary condition: prescribed T

The general formulas (1.2,1.3) with $T_0 = T_s$ and $z_0 = 0$ yield

$$\alpha_1 = \frac{\Delta t}{(\rho c)_1} \frac{k_{3/2}}{(z_2 - z_1)z_2} \quad \text{and} \quad \gamma_1 = \frac{\Delta t}{(\rho c)_1} \frac{k_{1/2}}{z_1 z_2}$$

The relation for $j = 1$ becomes

$$-\alpha_1 T_2^{n+1} + (1 + \alpha_1 + \gamma_1)T_1^{n+1} = \alpha_1 T_2^n + (1 - \alpha_1 - \gamma_1)T_1^n + \gamma_1(T_s^n + T_s^{n+1}) \quad (1.6)$$

which is implemented in `conductionT.f90`. This is a standard Crank-Nicolson solver for an irregular spaced grid.

1.1.3 Lower boundary condition

(assume $z_{N+1} - z_N = z_N - z_{N-1} =: \Delta z$)
No heat flux: $F_{N+\frac{1}{2}} = 0 \quad \Rightarrow \quad k_{N+\frac{1}{2}}(T_{N+1} - T_N) = 0 \quad \Rightarrow \quad T_{N+1} = T_N$

$$(1 + \gamma_N)T_N^{n+1} - \gamma_N T_{N-1}^{n+1} = (1 - \gamma_N)T_N^n + \gamma_N T_{N-1}^n$$

$$\gamma_N = \frac{\Delta t}{(\rho c)_N} \frac{k_{N-\frac{1}{2}}}{2(z_N - z_{N-1})^2}$$

With geothermal heating: $F_{N+\frac{1}{2}} = F_{\text{geothermal}} \quad \Rightarrow \quad k_{N+\frac{1}{2}}(T_{N+1} - T_N) = \Delta z F_{\text{geothermal}}$

$$(1 + \gamma_N)T_N^{n+1} - \gamma_N T_{N-1}^{n+1} = (1 - \gamma_N)T_N^n + \gamma_N T_{N-1}^n + \frac{\Delta t}{(\rho c)_N} \frac{F_{\text{geothermal}}}{\Delta z} \tag{1.7}$$

1.1.4 Validations

The following tests were performed for these solvers:

a) For a sinusoidally varying surface temperature, the solution to the heat equation is known analytically:

$$T = T_m + T_a e^{-z/\delta} \sin\left(\frac{z}{\delta} - \frac{2\pi t}{P}\right) \tag{1.8}$$

where

$$\delta = \frac{\Gamma}{\rho c}\sqrt{\frac{P}{\pi}} \tag{1.9}$$

is the thermal skin depth, Γ the thermal inertia, and P the period. This expression can be used to validate `conductionT` for uniform thermal properties (Figure 1.1). The heat flux is given by

$$F = -k\frac{\partial T}{\partial z} = -\sqrt{2}\, k \frac{T_a}{\delta} e^{-z/\delta} \cos\left(\frac{z}{\delta} - \frac{2\pi t}{P} + \frac{\pi}{4}\right)$$

b) Convergence of some solutions with Δt and Δz has been verified.

c) For periodic solutions (of `conductionT` and `conductionQ`) the heat flux $F = -k\partial T/\partial z$, time-averaged over one period, must be the same at all depths and equal to the heat flux imposed at the bottom boundary, even for spatially-varying thermal properties, as long as the heat capacity does not vary with time; consider the time average of eq. (1.1). Figure 1.2 shows one example.

d) A short-term solution for the heat equation with Stefan-Boltzmann radiation surface boundary condition was derived by Handelsman and Olmstead (1972). Their non-dimensional equations are $T_t = T_{zz}$, $T_z(0,t) = T^n(0,t) - f(t)$, $T(z,0) = 0$, $\lim_{z\to\infty} T(z,t) = 0$. In our case $n = 4$ and $f(t) = T_e^4$, where T_e is an ambient temperature. In this case, their
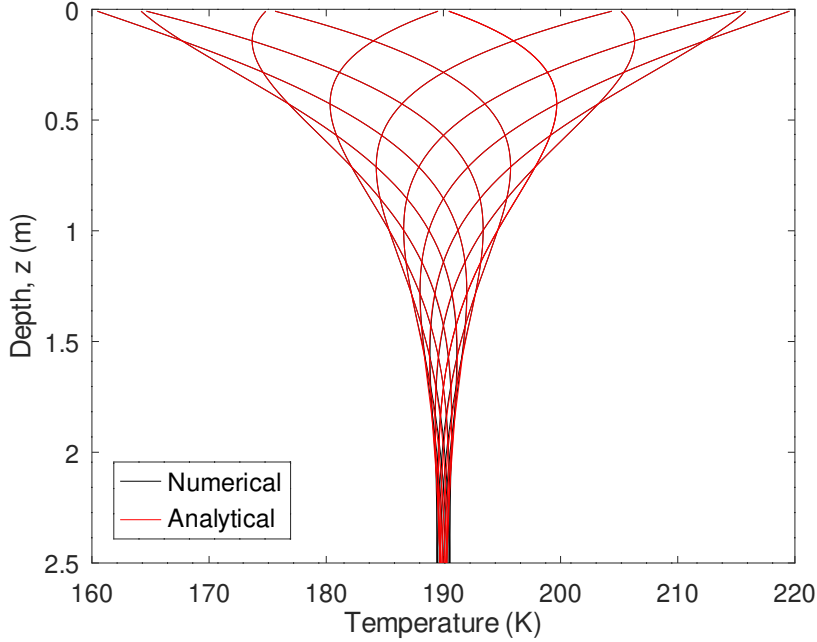
Figure 1.1: Comparison of numerical with analytical solution for Crank-Nicolson solver with periodic surface boundary condition. The deviations at the bottom are justified because the analytical solution (1.8) is for an infinitely deep domain. Non-equidistant grid points were used in this example.

solution is $T(0,t) = \frac{2}{\sqrt{\pi}} T_e^4 \sqrt{t}$, for small t. After re-dimensionalizing, the surface temperature is found to change as

$$T(0,t) = T_0 + \frac{2}{\sqrt{\pi}} \frac{\epsilon\sigma}{\Gamma} \left(T_e^4 - T_0^4\right) \sqrt{t} \qquad \text{for small } t \geq 0 \qquad (1.10)$$

where $T_0 = T(0,0)$ is the initial surface temperature. Figure 1.3 shows that the numerical solver reproduces the expected behavior for this discontinuous change in incoming flux.

e) When applied to Mars, modeled surface temperatures have been compared to TES (Thermal Emission Spectrometer) surface temperatures.

Table 1.1: Current implementations of 1D heat equation solvers. `conductionT/Q` are provided in four languages: Fortran, C, Matlab, and Python.

Subroutine	Description
`conductionT.f90`	standard Crank-Nicolson solver
`conductionQ.f90`	Crank-Nicolson with σT^4 emission at upper boundary
`conductionT2.f90`	version of `conductionT` that precomputes coefficients
`conductionQ2.f90`	version of `conductionQ` that precomputes coefficients
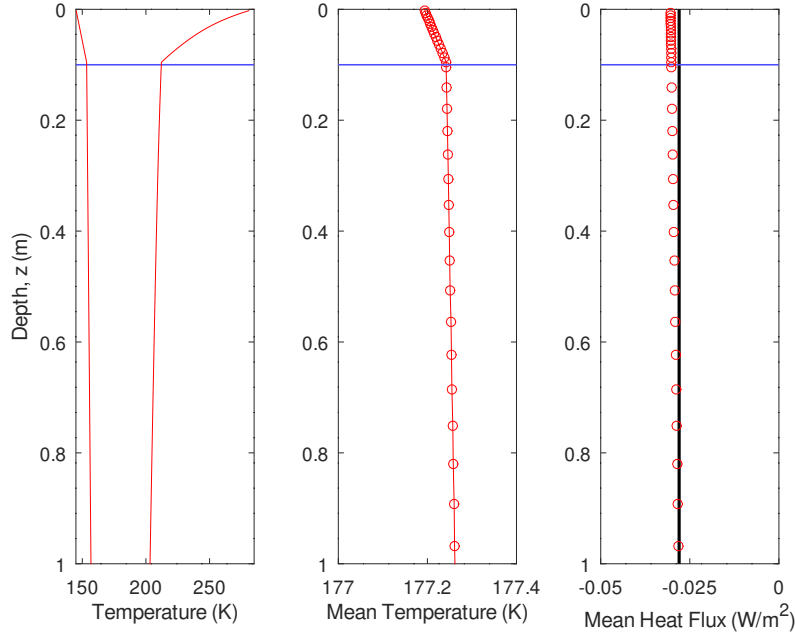
Figure 1.2: Validation of the conservation of the heat flux (flux-conservative discretization). The ice table at 10 cm depth causes dramatic changes in thermal properties. Left panel: Minimum and maximum subsurface temperatures over one Mars year. Middle panel: Temperatures averaged over one Mars year, which change linearly as the thermal conductivity is constant within each of the two layers. Right panel: Heat flux averaged over one Mars year, which is preserved across changes in thermal properties and equals to the heat flux imposed at the bottom boundary of 0.028 W/m^2.

1.2 Other Model Components

1.2.1 Seasonal frost cover (Mars)

The surface energy balance with the latent heat of CO_2 sublimation added is

$$Q + k \left.\frac{\partial T}{\partial z}\right|_{z=0} = \epsilon\sigma T^4|_{z=0} + L\frac{dm_{CO_2}}{dt} \quad \text{with} \quad m_{CO_2} \geq 0 \tag{1.11}$$

where L is the specific latent heat and m_{CO_2} is the areal density of CO_2 ice. Call `conductionQ` if the surface temperature T_s is above the CO_2 frost point temperature or if $m_{CO_2} = 0$. Call `conductionT` if T_s is below the CO_2 frost point or if $m_{CO_2} > 0$. In the latter case, calculate the energy difference and update m_{CO_2}. Adjust the surface albedo and infrared emissivity. Repeat this at every time step. `mars_thermal1d.f` is an implementation of the 1D thermal model for Mars.

1.2.2 Thermal properties of the ground

at around 200 Kelvin: $c_{ice} \approx 1540$ J/(kg K), $\rho_{ice} \approx 927$ kg/m^3, $k_{ice} \approx 3.2$ W/(m K)

9
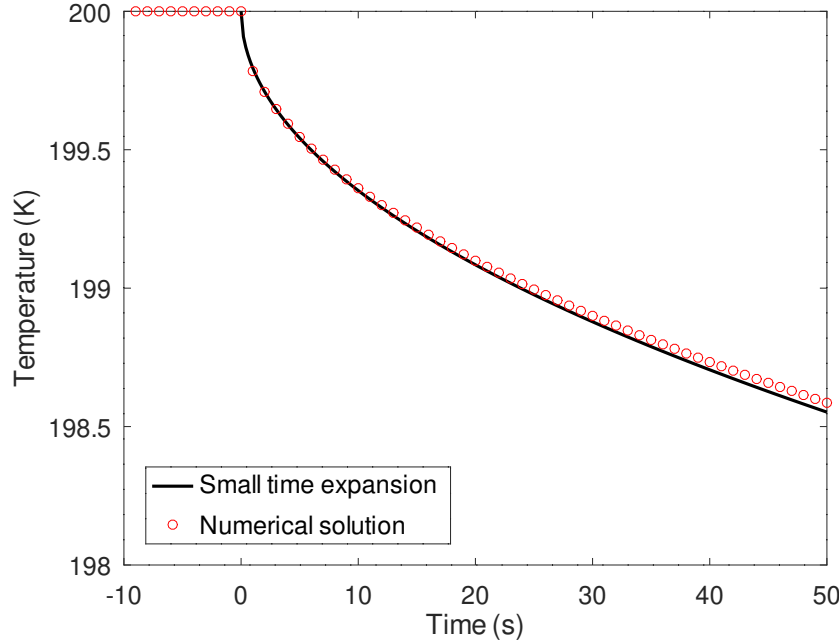
Figure 1.3: Response of numerical solution to a sudden change in incoming flux compared to the analytically obtained expansion for small times, eq. (1.10).

See Winter and Saari (1969) for heat capacity of silicates as a function of temperature. Notably, many silicates have about the same specific heat capacity. See Handbook of Chemistry and Physics (Lide, 2003) for the temperature dependence of ice.

The thermal conductivity varies by four orders of magnitudes on planetary surfaces, primarily due to the dependence on grain size. The parametrization of thermal conductivity in particulate soil is a vast subject. In the terrestrial context, Robertson (1988) provides an extensive compilation of the thermal properties of bulk rock.

Influence of ice on thermal properties: Ice can greatly change the thermal properties of porous ground. The following is one possible parametrization. In retrospective, it agrees well with the laboratory measurements by Siegler et al. (2012) for vapor-deposited ice.

$$\rho c = (1 - \epsilon)\rho_{\text{regolith}}c_{\text{regolith}} + \epsilon f \rho_{\text{ice}}c_{\text{ice}}$$
$$k = (1 - \epsilon)k_{\text{regolith}} + \epsilon f k_{\text{ice}} + (1 - f)\epsilon k_{\text{air}}$$

where ρ is density, c heat capacity, k thermal conductivity, ϵ porosity (void space / total volume), and f the ice filling fraction ($f = \rho_f/\rho_{\text{ice}}$, ρ_f =density of free ice).

In the program, k and ρc are defined halfway between grid points, whereas ρ_f and T are defined on grid points.

1.2.3 Incidence angle and orbits

The elevation β of the sun above an horizontal horizon is given in terms of geographic latitude λ, declination δ of the sun, and the hour angle h by

$$\sin \beta = \cos \lambda \cos \delta \cos h + \sin \lambda \sin \delta. \tag{1.12}$$

Table 1.2: Subroutines that provide sun positions.

Subroutine	Description
generalorbit.f	general ellipsoidal orbit (solves Kepler's equation with Newton method)
marsorbit.f90	orbit for present-day Mars
sunpos.f90	sun position for Earth

NASA's SPICE Toolkit provides the sun position for solar system bodies, and can be used instead of the subroutines listed in Table 1.2.

1.2.4 Mars atmospheric extinction and sky irradiance

The absorbed direct solar irradiance is approximately

$$Q_{\text{solar}} = \frac{S_0}{R^2}(1 - A)(1 - f)^{1/\max(\sin \beta, 0.04)} \sin \beta, \tag{1.13}$$

where S_0 is the solar constant, R the distance from the sun in AU, A the albedo, and f due to the extinction in the atmosphere. The length of the path through the atmosphere is approximately proportional to $1/\sin \beta$ and the transmission is taken to be exponential in this path length. The nadir optical depth of the atmosphere is $-\ln(1 - f) \approx f$. For small extinction and away from the horizon, $(1-f)^{1/\sin \beta} \approx 1-f/\sin \beta$. The maximum atmospheric path length $\ell_{\max}$ is limited due to the curvature of the planet, $H/\ell_{\max} \approx \sqrt{H/2R} \approx 0.04$ for Mars, where H is the scale height of the atmosphere and R the radius of the planet.

In addition to the direct insolation, the diffuse irradiance from the sky contributes to the surface energy balance (sky irradiance). Atmospheric emission is approximated by a fraction f_{IR} (typically 2–4%) of noontime insolation and is kept constant throughout a solar day (Kieffer et al., 1977):

$$Q_{\text{a,IR}} = f_{\text{IR}} \frac{S_0}{R^2} \sin \beta_{\text{noon}} \qquad \text{(all day)} \tag{1.14}$$

This approximation fails in the polar regions; in this case, Kieffer et al. (1977) replaces the noontime insolation with the surface frost emission.

In addition, there is scattered light when $\sin \beta > 0$, which is approximated by

$$Q_{\text{a,scat}} = \frac{1}{2} f_{\text{scat}} \frac{S_0}{R^2}. \tag{1.15}$$

Half of the scattered light is assumed to be lost to space.

11

For the purpose of discussion, we determine the total energy budget of the atmosphere for a horizontal land mass. To first order $(1 - f)^{1/\sin\beta} \sin\beta \approx \sin\beta - f$, in eq. (1.13), so at any time the sun is above the horizon the energy absorbed and scattered in the atmosphere is approximately $(S_0/R^2)f$. Over a solar day

$$\frac{S_0}{R^2} f \int_{\text{daytime}} dh \approx \frac{S_0}{R^2} \pi f. \tag{1.16}$$

The infrared emission from the atmosphere over the same time period is

$$2\pi f_{\text{IR}} \frac{S_0}{R^2} \sin\beta_{\text{noon}} \tag{1.17}$$

and the scattered energy

$$\pi f_{\text{scat}} \frac{S_0}{R^2}. \tag{1.18}$$

The globally averaged $\sin\beta_{\text{noon}}$ is

$$\frac{1}{\pi} \int_{-\pi/2}^{\pi/2} d\lambda \cos\lambda \sin\beta_{\text{noon}} \approx \frac{1}{\pi} \int_{-\pi/2}^{\pi/2} d\lambda \cos^2\lambda = \frac{1}{2} \tag{1.19}$$

Global balance, (1.16)=(1.17)+(1.18), is achieved with $f = f_{\text{IR}} + f_{\text{scat}}$. This relation does not hold at an individual latitude, but it does hold globally.

The Mars thermal model was used in Schorghofer and Aharonson (2005) and many subsequent papers, including Schorghofer (2008).

1.3 Semi-Implicit Scheme for Spherically Symmetric Geometry

History: developed 2018–2019

Governing equation (1.1) is appropriate for depths small compared to the radius of the body. In the context of small asteroids, it may be necessary to include the curvature effect. A one-dimensional spherically-symmetric semi-implicit heat solver has been implemented (subroutine `conductionT_sphere` in `sphere1d_implicit.f90`). Conceptually, the derivation is the same as in section 1.1. The implementation is limited to constant grid spacing, uniform thermal properties, and a temperature boundary condition on the surface.

The equation for energy conservation in three dimensions is

$$\rho c \frac{\partial T}{\partial t} - \vec{\nabla} \cdot (k \vec{\nabla} T) = 0 \tag{1.20}$$

In the spherically symmetric (1D) case, this equation becomes

$$\rho c \frac{\partial T}{\partial t} = \frac{1}{r^2} \frac{\partial}{\partial r} \left(k r^2 \frac{\partial T}{\partial r} \right)$$

For spatially uniform k, this simplifies to

$$\frac{\partial T}{\partial t} = \frac{\kappa}{r^2}\frac{\partial}{\partial r}\left(r^2\frac{\partial T}{\partial r}\right) \tag{1.21}$$

where $\kappa = k/(\rho c)$ is the thermal diffusivity.

The upper (surface) boundary condition is prescribed as a time-dependent temperature $T_0(t)$, which may in turn be obtained from a separate model based on the orbital and physical parameters of the body. At the center of the body $\partial T/\partial r = 0$, which forms the lower boundary condition.

To achieve a spatial discretization that conserves the heat flux, center differences are applied to the equation in the form of (1.21). It would be a mistake to apply the chain rule of differentiation and then discretize. The term in the parenthesis is

$$\left(r^2\frac{\partial T}{\partial r}\right)_j = r_j^2\frac{T_{j+1/2} - T_{j-1/2}}{\Delta r}$$

The discretization of the right-hand side of equation (1.21) is:

$$(\text{rhs})_j = \frac{\kappa}{r_j^2(\Delta r)^2}\left[r_{j+1/2}^2 T_{j+1} - \left(r_{j+1/2}^2 + r_{j-1/2}^2\right)T_j + r_{j-1/2}^2 T_{j-1}\right]$$

Introduce $c_{j+1/2} = (r_{j+1/2}/r_j)^2$, $c_{j-1/2} = (r_{j-1/2}/r_j)^2$, and $c_j = (c_{j+1/2} + c_{j-1/2})/2$, then this abbreviates to

$$(\text{rhs})_j = \frac{\kappa}{(\Delta r)^2}\left[c_{j+1/2} T_{j+1} - 2c_j T_j + c_{j-1/2} T_{j-1}\right]$$

For an explicit scheme

$$\frac{T_j^{n+1} - T_j^n}{\Delta t} = (\text{rhs})_j^n$$

where the superscripts enumerate time steps. For a semi-implicit (Crank-Nicolson) scheme

$$\frac{T_j^{n+1} - T_j^n}{\Delta t} = \frac{1}{2}(\text{rhs})_j^n + \frac{1}{2}(\text{rhs})_j^{n+1} \tag{1.22}$$

It is useful to introduce the abbreviation

$$\alpha = \kappa\frac{\Delta t}{(\Delta r)^2}$$

For the semi-implicit scheme (1.22),

$$T_j^{n+1} - \frac{\alpha}{2}\left[c_{j+1/2}T_{j+1}^{n+1} - 2c_j T_j^{n+1} + c_{j-1/2}T_{j-1}^{n+1}\right] = T_j^n + \frac{\alpha}{2}\left[c_{j+1/2}T_{j+1}^n - 2c_j T_j^n + c_{j-1/2}T_{j-1}^n\right]$$

From this results the linear system of equations

$$-\frac{\alpha}{2}c_{j+1/2}T_{j+1}^{n+1} + (1 + \alpha c_j)T_j^{n+1} - \frac{\alpha}{2}c_{j-1/2}T_{j-1}^{n+1} = +\frac{\alpha}{2}c_{j+1/2}T_{j+1}^n + (1 - \alpha c_j)T_j^n + \frac{\alpha}{2}c_{j-1/2}T_{j-1}^n \tag{1.23}$$

which is solved numerically by tridiagonal inversion.

At the upper boundary, the temperature T_0 is prescribed. For $j = 1$, equation (1.23) becomes

$$-\frac{\alpha}{2}c_{3/2}T_2^{n+1} + (1+\alpha c_1)T_1^{n+1} = +\frac{\alpha}{2}c_{3/2}T_2^n + (1-\alpha c_1)T_1^n + \frac{\alpha}{2}c_{1/2}(T_0^n + T_0^{n+1}) \qquad (1.24)$$

For the lower boundary condition, at the center of the sphere ($j = N$): $\partial T/\partial r = 0$ and therefore $T_{N+1} = T_{N-1}$. Equation (1.23) would then be

$$(1+\alpha c_N)T_N^{n+1} - \alpha c_N T_{N-1}^{n+1} = (1-\alpha c_N)T_N^n + \alpha c_N T_{N-1}^n \qquad (1.25)$$

However, c_N is ill-defined at $r_N = 0$. At the center, $T(r) = T(0) + \beta r^2/2$. Hence, $\partial T/\partial r = \beta r$ and $\partial^2 T/\partial r^2 = \beta$. The divergence of the temperature is

$$\nabla^2 T = \frac{1}{r^2}\frac{\partial}{\partial r}\left(r^2\frac{\partial T}{\partial r}\right) = \frac{2}{r}\frac{\partial T}{\partial r} + \frac{\partial^2 T}{\partial r^2} = \frac{2}{r}\beta r + \beta = 3\beta = 3\frac{\partial^2 T}{\partial r^2}$$

The divergence at the center can thus be evaluated as

$$(\nabla^2 T)_N = 3\frac{T_{N+1} - 2T_N + T_{N-1}}{(\Delta r)^2} = 6\frac{-T_N + T_{N-1}}{(\Delta r)^2}$$

and $(\text{rhs})_N$ is κ times this divergence. The lower boundary condition for the semi-implicit scheme becomes

$$(1+3\alpha)T_N^{n+1} - 3\alpha T_{N-1}^{n+1} = (1-3\alpha)T_N^n + 3\alpha T_{N-1}^n \qquad (1.26)$$

In other words, $c_N = 3$, in equation (1.25). For comparison, $c_{N-1} = 5/4$.

Bibliography

Crank, J. and Nicolson, P., 1947. A practical method for numerical evaluation of solutions of partial differential equations of the heat-conduction type. *Mathematical Proceedings of the Cambridge Philosophical Society* 43(1):50–67.

Handelsman, R. A. and Olmstead, W. E., 1972. Asymptotic solution to a class of nonlinear Volterra integral equations. *SIAM J. Appl. Math.* 22(3):373–384. doi: 10.1137/0122035.

Kieffer, H. H., Martin, T. Z., Peterfreund, A. R., Jakosky, B. M., Miner, E. D., and Palluconi, F. D., 1977. Thermal and albedo mapping of Mars during the Viking primary mission. *J. Geophys. Res.* 82(28):4249–4291. doi: 10.1029/JS082i028p04249.

Lide, D. R., editor, 2003. *CRC Handbook of Chemistry and Physics.* CRC Press, 84th edition.

Press, W. H., Teukolsky, S. A., Vetterling, W. T., and Flannery, B. P., 1992. *Numerical Recipes in C.* Cambridge University Press, New York, second edition.

Robertson, E. C., 1988. Thermal properties of rocks. Technical report, US Geological Survey. Open-File Report 88-441, 110pp.

Schorghofer, N., 2008. Temperature response of Mars to Milankovitch cycles. *Geophys. Res. Lett.* 35:L18201. doi: 10.1029/2008GL034954.

Schorghofer, N. and Aharonson, O., 2005. Stability and exchange of subsurface ice on Mars. *J. Geophys. Res.* 110(E5):E05003. doi: 10.1029/2004JE002350.

Siegler, M., Aharonson, O., Carey, E., Choukroun, M., Hudson, T., Schorghofer, N., and Xu, S., 2012. Measurements of thermal properties of icy Mars regolith analogs. *J. Geophys. Res.* 117:E03001. doi: 10.1029/2011JE003938.

Winter, D. F. and Saari, J. M., 1969. A particulate thermophysical model of the lunar soil. *Astrophys. J.* 156:1135–1151.

Part 2

Diffusion of Water Vapor with Phase Transitions

1-Dimensional Diffusion of Water Vapor in Porous Medium with Phase Transitions;
variable diffusivity; irregular grid
3 phases: vapor, free (macroscopic) H_2O ice, H_2O adsorbate
implemented in `vapordiffusioni.f`

History: developed 2003–2004

2.1   Governing Equations

indices: v ... gas (vapor), f ... free ice (solid), a ... adsorbed water
$\bar{\rho}$ ... mass per total volume, $\bar{J}$ ... vapor flux per total area

conservation of mass:
$$\frac{\partial}{\partial t}(\bar{\rho}_v + \bar{\rho}_f + \bar{\rho}_a) + \nabla \cdot \bar{J} = 0 \tag{2.1}$$

vapor transport: (Landau and Lifshitz, 1987, Vol. VI, §57, §58)

$$J = -D\rho_0 \nabla c \tag{2.2}$$

c ... concentration $c = \rho_v/\rho_0$
ρ_0 ... total density of air, including water vapor
ρ_v ... density of vapor

$$p_v = nkT = \rho_v \frac{k}{m_v} T \tag{2.3}$$

m_v ... mass of water molecule; k ... Boltzmann constant

ϵ ... porosity (= void space / total volume)
$\epsilon(1 - \rho_f/\rho_{\text{ice}})$ ... fraction of space available to gas
$\bar{\rho}_v = \rho_v \epsilon(1 - \rho_f/\rho_{\text{ice}})$ ρ_v ... vapor density in void space
$\bar{\rho}_f = \rho_f \epsilon$ ρ_f ... ice density in volume not occupied by regolith
$\bar{J} = J\epsilon(1 - \rho_f/\rho_{\text{ice}})$ J ... vapor flux through void area
$\rho_{\text{ice}} \approx 926$ kg/m^3 ... density of ice when it's really cold

adsorption: $\bar{\rho}_a = A(p, T)$ reversible and not kinetically-limited

Conservation of mass becomes

$$\frac{\partial}{\partial t}\left(\rho_v\left(1 - \frac{\rho_f}{\rho_{\text{ice}}}\right) + \rho_f + \frac{1}{\epsilon}\bar{\rho}_a\right) + \partial_z\left(1 - \frac{\rho_f}{\rho_{\text{ice}}}\right)J = 0$$

$$\frac{\partial}{\partial t}\left[\rho_v\left(1 - \frac{\rho_f}{\rho_{\text{ice}}}\right) + \rho_f + \frac{1}{\epsilon}\bar{\rho}_a\right] = \partial_z\left[\left(1 - \frac{\rho_f}{\rho_{\text{ice}}}\right)D\partial_z\rho_v\right]$$

introduce $\varphi = 1 - \dfrac{\rho_f}{\rho_{\text{ice}}}$ and $\gamma = \dfrac{k}{m}\dfrac{1}{\epsilon}$

$$\partial_t\left(\frac{p}{T}\varphi + \frac{k}{m_v}\rho_f\right) + \gamma\left(\frac{\partial\bar{\rho}_a}{\partial p}\partial_t p + \frac{\partial\bar{\rho}_a}{\partial T}\partial_t T\right) = \partial_z\left[D\varphi\left(\partial_z\frac{p}{T}\right)\right] \tag{2.4}$$

This is an equation for p and ρ_f.

If there is no ice, then

$$\left(\frac{1}{T} + \gamma\frac{\partial\bar{\rho}_a}{\partial p}\right)\partial_t p + \left(-\frac{p}{T^2} + \gamma\frac{\partial\bar{\rho}_a}{\partial T}\right)\partial_t T = \partial_z\left(D\partial_z\frac{p}{T}\right)$$

2.2 Discretizations

2.2.1 Possible discretizations of spatial derivatives

Note: These spatial discretizations are not necessarily optimal in terms of discretization error.

$$\partial_z(a\partial_z b)|_j = \frac{1}{\Delta z^2}\left(a_{j+1/2}(b_{j+1} - b_j) - a_{j-1/2}(b_j - b_{j-1})\right) + O(\Delta z^2) \tag{2.5}$$

or

$$\partial_z(a\partial_z b)|_j = \frac{1}{2\Delta z^2}\left((a_{j+1} + a_j)(b_{j+1} - b_j) - (a_j + a_{j-1})(b_j - b_{j-1})\right) + O(\Delta z^2) \tag{2.6}$$

or

$$\partial_z(a\partial_z b)|_j = a\partial_{zz}b + (\partial_z a)\partial_z b$$
$$= \frac{1}{\Delta z^2}\left[a_j(b_{j+1} - 2b_j + b_{j-1}) + \frac{1}{4}(a_{j+1} - a_{j-1})(b_{j+1} - b_{j-1})\right] + O(\Delta z^2) \tag{2.7}$$

The most general discretization which is accurate to $O(\Delta z^2)$, rather than just $O(\Delta z)$, is of the following form (mathematica notebook discretization2.nb)

$$\begin{aligned}
\partial_z(a\partial_z b)|_j = &\frac{1}{\Delta z^2}(ca_j b_j + (-1 - \frac{c}{2})a_{j-1}b_j + (-1 - \frac{c}{2})a_{j+1}b_j \\
&- \frac{c}{2}a_j b_{j-1} + \frac{3+c}{4}a_{j-1}b_{j-1} + \frac{1+c}{4}a_{j+1}b_{j-1} \\
&- \frac{c}{2}a_j b_{j+1} + \frac{1+c}{4}a_{j-1}b_{j+1} + \frac{3+c}{4}a_{j+1}b_{j+1}) + O(\Delta z^2)
\end{aligned} \tag{2.8}$$

Choices (2.6) and (2.7) above correspond to $c = -1$ and $c = -2$, respectively.

Another set of schemes does not involve the cross-terms $a_{j+1}b_{j-1}$ and $a_{j-1}b_{j+1}$. They are of the following form (mathematica notebook discretization3.nb)

$$
\begin{aligned}
\partial_z(a\partial_z b)|_j &= \frac{1}{\Delta z^2}(-a_j b_j - c a_{j-1} b_j + (-1+c)a_{j+1}b_j + \\
&\quad (1-c)a_j b_{j-1} + c a_{j-1}b_{j-1} + c a_j b_{j+1} + (1-c)a_{j+1}b_{j+1}) + \\
&\quad \left(c - \frac{1}{2}\right) O(\Delta z) + O(\Delta z^2) \\
&= \frac{1}{\Delta z^2}[(1-c)a_{j+1}(b_{j+1} - b_j) + c a_{j-1}(b_{j-1} - b_j) + \\
&\quad + a_j(c b_{j+1} - b_j + (1-c)b_{j-1})] + O(\Delta z)
\end{aligned}
\tag{2.9}
$$

For $c = 1/2$ this reduces to scheme (2.6) above
If starting with complete pore filling, $c > 0$ is required for downward motion of ice table.

On irregular grid: General scheme without cross-terms (mathematica notebook discretization6.nb)

$$
\begin{aligned}
\partial_z(a\partial_z b)|_j &= -\frac{2c + (1-2c)h_+/h_-}{h_- h_+}a_j b_j + \frac{-1 + (1-2c)h_+/h_-}{h_-(h_- + h_+)}a_{j-1}b_j + \frac{2c - 2}{h_+(h_- + h_+)}a_{j+1}b_j + \\
&\quad + \frac{1 + (1-2c)h_+/h_-}{h_-(h_- + h_+)}a_j b_{j-1} + \frac{1 + (2c-1)h_+/h_-}{h_-(h_- + h_+)}a_{j-1}b_{j-1} + \frac{2c}{h_+(h_- + h_+)}a_j b_{j+1} \\
&\quad + \frac{2 - 2c}{h_+(h_- + h_+)}a_{j+1}b_{j+1} + O(h_+ + h_-)
\end{aligned}
\tag{2.10}
$$

where $h_+ = z_{j+1} - z_j$ and $h_- = z_j - z_{j-1}$. For $h_+ = h_- = h$ this reduces to (2.9)

2.2.2 Discretization of time derivative

use eq. (2.4), $A \equiv f$

$$
\begin{aligned}
\frac{p_j^{n+1}}{T_j^{n+1}}\varphi_j^{n+1} - \frac{p_j^n}{T_j^n}\varphi_j^n + \frac{k}{\mu}\left(\rho f_j^{n+1} - \rho f_j^n\right) + \gamma \left.\frac{\partial f}{\partial p}\right|_j^n (p_j^{n+1} - p_j^n) + \\
+ \gamma \left.\frac{\partial f}{\partial T}\right|_j^n (T_j^{n+1} - T_j^n) = \Delta t \left(\partial_z D\varphi \partial_z \frac{p}{T}\right)_j^n
\end{aligned}
\tag{2.11}
$$

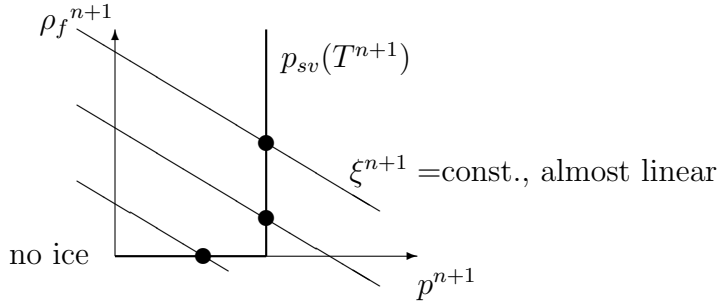derivatives of the isotherm are not expanded to keep it linear

2.2.3   Complete scheme

using (2.11) and (2.10)

$$
\begin{aligned}
\xi_j^{n+1} &= \frac{p_j^n}{T_j^n}\varphi_j^n + \frac{k}{\mu}\rho_{f\,j}^n + \gamma\left.\frac{\partial f}{\partial p}\right|_j^n p_j^n - \gamma\left.\frac{\partial f}{\partial T}\right|_j^n (T_j^{n+1}-T_j^n) + \\
&\quad \frac{\Delta t}{\Delta z^2}\left[D_j\varphi_j^n\left(\frac{p_{j+1}^n}{T_{j+1}^n}-2\frac{p_j^n}{T_j^n}+\frac{p_{j-1}^n}{T_{j-1}^n}\right)+\frac{1}{4}(D_{j+1}\varphi_{j+1}^n-D_{j-1}\varphi_{j-1}^n)\left(\frac{p_{j+1}^n}{T_{j+1}^n}-\frac{p_{j-1}^n}{T_{j-1}^n}\right)\right]
\end{aligned}
$$

where $\xi^{n+1} = \dfrac{p^{n+1}}{T^{n+1}}\left(1-\dfrac{\rho_f^{n+1}}{\rho_{\text{ice}}}\right)+\dfrac{k}{\mu}\rho_f^{n+1}+\gamma\left.\dfrac{\partial f}{\partial p}\right|^n p^{n+1}$

$p \le p_{sv}(T)$ and $0 \le \rho_f \le \rho_{\text{ice}}$

p_{sv} ... saturation vapor pressure

Try $\rho_f^{n+1}=0 \quad\Rightarrow\quad p^{n+1}=\dfrac{T^{n+1}\cdot\xi^{n+1}}{1+T^{n+1}\gamma\left.\frac{\partial f}{\partial p}\right|^n}$ and $\rho_f^{n+1}=0$

If $p^{n+1} > p_{sv}(T^{n+1})$ then $p^{n+1}=p_{sv}(T^{n+1})$ and

$$
\rho_f^{n+1}=\frac{\xi^{n+1}-\frac{p_{sv}(T^{n+1})}{T^{n+1}}-\gamma\left.\frac{\partial f}{\partial p}\right|^n p_{sv}(T^{n+1})}{\frac{k}{\mu}-\frac{p_{sv}(T^{n+1})}{T^{n+1}\rho_{\text{ice}}}}
$$

introduce $p_{\text{frost}}^{n+1}=p_{sv}(T^{n+1})$

2.2.4   Upper boundary condition

1) $p(z=0,t)=p_{\text{atm.}}(t)$
2) $D(z=0)=D_0$
3) $\varphi_0=1$

$$
\partial_z\left(D\varphi\partial_z\frac{p}{T}\right)\bigg|_{j=0}=\frac{1}{\Delta z^2}\left[D_1\varphi_1\left(\frac{p_2}{T_2}-2\frac{p_1}{T_1}+\frac{p_{\text{atm}}}{T_{\text{surf}}}\right)+\frac{1}{4}(D_2\varphi_2-D_0\varphi_0)\left(\frac{p_2}{T_2}-\frac{p_{\text{atm}}}{T_{\text{surf}}}\right)\right]
\tag{2.12}
$$

for half-shifted grid ($z_2 = 3z_1$):

$$a\partial_{zz}b + (\partial_z a)\partial_z b = \frac{1}{\Delta z^2}\left[a_1\left(\frac{8}{3}b_s - 4b_1 + \frac{4}{3}b_2\right) + \left(-\frac{4}{3}a_s + a_1 + \frac{1}{3}a_2\right)\left(-\frac{4}{3}b_s + b_1 + \frac{1}{3}b_2\right)\right]$$
(2.13)

2.2.5 Lower boundary condition

no vapor flux (impermeable) $J = 0 \quad \Rightarrow \quad \partial_z \rho_v = 0 \quad \Rightarrow \quad \partial_z \frac{p}{T} = 0 \quad \Rightarrow \quad \frac{p_{N+1}}{T_{N+1}} = \frac{p_{N-1}}{T_{N-1}}$

$$\partial_z\left(D\varphi\partial_z\frac{p}{T}\right)\Big|_{j=N} = \frac{1}{\Delta z^2}2D_N\varphi_N\left(\frac{p_{N-1}}{T_{N-1}} - \frac{p_N}{T_N}\right)$$
(2.14)

2.3 Discussion

For 1D diffusion and advection with multiple gases, the governing equations are more complex, but the numerical implementation is not. For the governing equations in non-isothermal environments see works such as Cunningham and Williams (1980); Bouziani and Fanale (1998); Hudson et al. (2007).

Water vapor diffusion calculations for Mars are carried out in Schorghofer and Aharonson (2005).

Bibliography

Bouziani, N. and Fanale, F. P., 1998. Physical chemistry of a heterogeneous medium: Transport processes in comet nuclei. *Astrophys. J.* 499(1):463. doi: 10.1086/305599.

Cunningham, R. and Williams, R., 1980. *Diffusion in Gases and Porous Media*. Plenum Press, New York.

Hudson, T. L., Aharonson, O., Schorghofer, N., Farmer, C. B., Hecht, M. H., and Bridges, N. T., 2007. Water vapor diffusion in Mars subsurface environments. *J. Geophys. Res.* 112(E5):E05016. doi: 10.1029/2006JE002815.

Landau, L. D. and Lifshitz, E. M., 1987. *Fluid Mechanics*. Pergamon Press, Oxford.

Schorghofer, N. and Aharonson, O., 2005. Stability and exchange of subsurface ice on Mars. *J. Geophys. Res.* 110(E5):E05003. doi: 10.1029/2004JE002350.

Part 3

Long-Term Ice Evolution

Long-term evolution of sub-surface ice due to loss to space (for asteroids), vapor exchange with the atmosphere (for Mars), or exchange with adsorbed H_2O (on the Moon) using diurnally- and seasonally-resolved temperatures.

History:
  2002–2004 equilibrium ice table on Mars
  2006–2011 asynchronous model for ice on Mars (where re-charge can occur)
  2013 & 2021 lunar thermal ice pump
  2013–2017 asynchronous model for asteroids (where impact-gardening occurs)

3.1   Equilibrium Ice Table on Mars

The equilibrium depth to the ice table is defined by a balance between the vapor pressure at the ice table and the atmosphere (Fig. 3.1). It is the end result of atmosphere-subsurface vapor exchange after an asymptotically long time. If no equilibrium is possible, then subsurface ice is "unstable". Using the thermal model described in Part 1, this model calculates the equilibrium depth based on matching the vapor density at the ice table with that in the atmosphere. The thermal model is run over a number of Mars years to equilibrate, and annual means are calculated for the last orbit. The ice content of the subsurface changes the thermal properties, and the thermal model is repeatedly equilibrated.
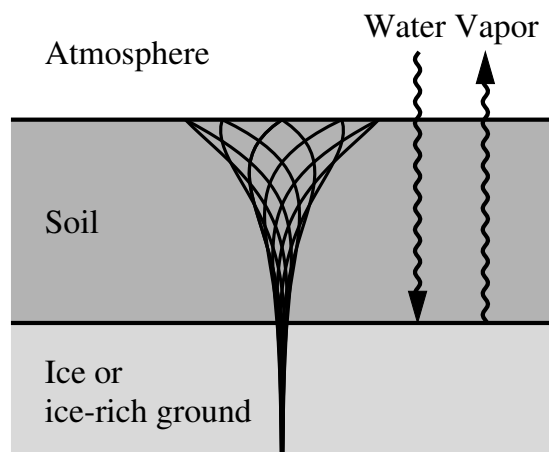

Figure 3.1: Subsurface ice exchanges water vapor with the atmosphere through a layer of porous soil. Temperature oscillations decay with depth, as illustrated by a set of instantaneous temperature profiles.

21

Figure 3.2 shows the result of thermal model calculations (using the methods described in Part 1) and vapor diffusion calculations (using the methods described in Part 2). The gradient in temperature changes at the ice table due to the change in thermal properties (Fig. 3.2a). The annual mean of the vapor density profile can be determined from the annual mean of the vapor density on the surface and at the ice table (Fig. 3.2c). The time-averaging can be justified mathematically by swapping the time integral with the gradient in Fick's diffusion law. These boundary values can be calculated without solving the vapor diffusion equation, which provides a major computational advantage.
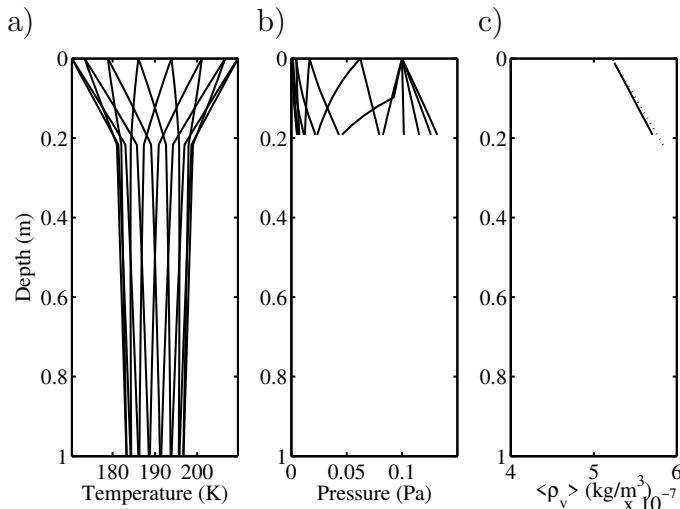
Figure 3.2: Temperature, partial pressure of H_2O, and annual mean vapor density $\langle \rho_v \rangle$ when the ice table is above equilibrium (and therefore retreats). In this conceptional example, a sinusoidal surface temperature dependence is assumed. The vapor density profiles vary with time, but the annual mean of ρ_v simply increases linearly with depth. The dotted line is based on the boundary values of the mean annual vapor density and closely approximates the annual mean from the microphysical vapor diffusion calculations.

The equilibrium ice table calculations determine at what depth the annual mean vapor density at the ice table matches that on the surface. Because the ice content changes the thermal properties, multiple thermal model runs need to be carried out to arrive at the equilibrium depth. A root-finding procedure is deployed to find the equilibrium depth. In `mars_mapi.f` the root-finding procedure is a bisection method. The more recent but simpler program `mars_mapii.f` instead iteratively updates the instantaneous equilibrium depth to arrive at the unique final equilibrium depth. Then `mars_mapt.f` can be used to output additional variables for a given ice table depth.

The model was extensively used in Schorghofer and Aharonson (2005), where further description is available. With extensions described in section 5.2 for planar slopes, it also forms the core of the model used in Aharonson and Schorghofer (2006).

Table 3.1: Programs that calculate the equilibrium ice table on Mars.

Main program	Task
mars_mapt	temperatures for prescribed ice table depth
mars_mapi	finds equilibrium ice table with bisection method
mars_mapii	finds equilibrium ice table with iteration method
mars_mapi2p	finds equilibrium ice table for planar slopes with bisection method

3.2 Asynchronous Model for Near-Surface Ice on Mars

The model couples a diurnally-resolved thermal model with a long-term ice evolution model. Ice (massive or interstitial) can be lost to the atmosphere and, vice-versa, pore spaces can be recharged with interstitial ice. In difference to the model for the equilibrium ice table (section 3.1), this *dynamical* model calculates changes in ice volume and the interstitial spaces may only be partially filled with ice.

Schorghofer (2010) provides a description of this rather complex model, which is not repeated here. In brief, the time-averaged vapor transport equations are solved, which avoids having to solve the microphysical vapor transport equations. The numerical method involves a one-sided derivative at the moving ice table, otherwise a numerical instability occurs due to the strong contrast in thermal properties at the ice table. The model allows for up to three layers: ice-free, soil with interstitial ice (plus void spaces), and massive ice with dust. In the current implementation, one of the two interfaces is tracked explicitly. The model is extensively used in Schorghofer (2007) and Schorghofer and Forget (2012) for studies of the Martian Ice Age cycle.

Table 3.2: Overview of current implementations of asynchronous dynamic models

Main program	Task
mars_fast	ice evolution on Mars (massive and interstitial ice)
exper_fast	ice evolution in lab experiment
stabgrow_fast	growth of pore ice
asteroid_fast1	temperature, ice loss, collapsed sublimation lag
asteroid_fast2	temperature, ice loss, impact mixing

3.3 Asynchronous Model for Temperature, Impact Mixing, and Ice Loss on Asteroids

Schorghofer (2016) describes this model and applies it to (1) Ceres and (7968) Elst-Pizarro. In brief, it combines diurnally-resolved temperatures, probabilistic impact stirring (only one-dimensional), and the long-term loss of near-surface ice to space due to sublimation and diffusion. It was also used for the ice retreat calculations published in Prettyman et al. (2017). The solar constant gradually increases according to the standard solar evolution model (Gough, 1981). The main program is asteroid_fast2.

A significant complexity in this model arises from partially ice-filled pore spaces (necessary to incorporate the consequences of impact stirring), because the re-distribution of ice within the pores due to vapor diffusion and deposition adds another governing equation. This redistribution turned out to be negligible in all cases it was considered. A simpler two-layer version, where pore spaces are either empty or full, is implemented in `asteroid_fast1`, which is very similar to the model described in the supporting information of Sizemore et al. (2017).

Another application of asynchronous coupling is ice loss calculations for asteroids on dynamical orbits, that is, the orbital elements change over time (and continuous-time integration would be too slow). In Schorghofer et al. (2020) this computational method was applied to (potentially ice-rich) asteroids that originate in the Outer Main Belt.

3.4 Lunar Thermal Ice Pump

The concept of downward "pumping" of vapor by periodic temperature cycles, originally developed for Mars, can also be applied to the Moon, as described in Schorghofer and Taylor (2007); Schorghofer and Aharonson (2014). The governing equations are cast in the form of a boundary value problem, that is, by calculating the mobility of H_2O molecules on the surface and at one specific depth.

One component of these calculations is a model for the surface population of adsorbed water molecules. It involves a stiff differential equation that is solved with a simple implicit method (a backward Euler step). The "bottom point" is the ice table, or, for the purpose of determining whether or not pumping occurs, the depth of minimum sublimation rate, which is estimated by the sublimation rate at time-averaged temperature. Program `oscidea1.f90` is a simple driver program for the ice pump calculations. This model was used in Schorghofer and Aharonson (2014) and Schorghofer and Williams (2020). In the more recent work by Schorghofer (2022), the upper boundary condition has a fixed value instead (`moon_subsdiff_equilbr.f90`).

For the "adsorbate pump", the pumping is too weak for ice sequestration, but the pumping nevertheless causes an increase of adsorbate concentration with depth. Subsurface residence times depend not only on temperature but also on adsorbate density, which requires nonlinear root-finding, in addition to the surface population model.

Bibliography

Aharonson, O. and Schorghofer, N., 2006. Subsurface ice on Mars with rough topography. *J. Geophys. Res.* 111(E11):E11007. doi: 10.1029/2005JE002636.

Gough, D. O., 1981. Solar interior structure and luminosity variations. *Solar Physics* 74: 21–34. doi: 10.1007/978-94-010-9633-1_4.

Prettyman, T. H. et al., 2017. Extensive water ice within Ceres' aqueously altered regolith: Evidence from nuclear spectroscopy. *Science* 355:55–59. doi: 10.1126/science.aah6765.

Schorghofer, N., 2007. Dynamics of ice ages on Mars. *Nature* 449(7159):192–194. doi: 10.1038/nature06082.

Schorghofer, N., 2010. Fast numerical method for growth and retreat of subsurface ice on Mars. *Icarus* 208(2):598–607. doi: 10.1016/j.icarus.2010.03.022.

Schorghofer, N., 2016. Predictions of depth-to-ice on asteroids based on an asynchronous model of temperature, impact stirring, and ice loss. *Icarus* 276:88–95. doi: 10.1016/j.icarus.2016.04.037.

Schorghofer, N., 2022. Gradual sequestration of water at lunar polar conditions due to temperature cycles. *Astrophys. J. Lett.* 927(2):L34. doi: 10.3847/2041-8213/ac5a48.

Schorghofer, N. and Aharonson, O., 2005. Stability and exchange of subsurface ice on Mars. *J. Geophys. Res.* 110(E5):E05003. doi: 10.1029/2004JE002350.

Schorghofer, N. and Aharonson, O., 2014. The lunar thermal ice pump. *Astrophys. J.* 788:169. doi: 10.1088/0004-637X/788/2/169.

Schorghofer, N. and Forget, F., 2012. History and anatomy of subsurface ice on Mars. *Icarus* 220(2):1112–1120. doi: 10.1016/j.icarus.2012.07.003.

Schorghofer, N. and Taylor, G. J., 2007. Subsurface migration of H2O at lunar cold traps. *J. Geophys. Res.* 112(E2):E02010. doi: 10.1029/2006JE002779.

Schorghofer, N. and Williams, J.-P., 2020. Mapping of ice storage processes on the Moon with time-dependent temperatures. *Planet. Sci. J.* 1:54. doi: 10.3847/PSJ/abb6ff.

Schorghofer, N., Hsieh, H. H., Novakovic, B., and Walsh, K. J., 2020. Preservation of ice at the polar regions of near-earth asteroids originating in the outer main asteroid belt: A model study with dynamical trajectories. *Icarus* 348:113865. doi: 10.1016/j.icarus.2020.113865.

Sizemore, H. G. et al., 2017. Pitted terrain on dwarf planet Ceres and implications for volatiles. *Geophys. Res. Lett.* 44(13):6570–6578. doi: 10.1002/2017GL073970.

Part 4

Terrestrial Analogs

Terrestrial Atmospheric Absorption and Sky Irradiance

History: developed around 2013–2016

Sun position as a function of date is based on Blanco-Muriel et al. (2001), translated into Fortran. It provides the zenith angle and azimuth of the sun, and the Earth-sun distance. Implemented in `sunpos.f90`

4.1 Mauna Kea atmosphere

Clear-sky direct and indirect short-wave irradiance (W/m^2) on Mauna Kea, Hawaii
Parametrizations in the atmospheric model are mostly based on Nunez (1980), corrected for typos. Implemented in `mk_atmosphere.f90`

Z ... solar zenith angle (radians)
I_0 ... clear-sky direct irradiance; D_0 ... clear-sky diffuse irradiance
R ... Earth-sun distance in AU
m, m' ... optical air mass (unitless)
p_0 ... total pressure (Pa)
w ... precipitable water vapor (cm)
Transmission coefficients:
ψ_{wa} ... water vapor absorption; ψ_{ws} ... water vapor scattering
ψ_{rs} ... Rayleigh scattering
ψ_{da} ... dust absorption; ψ_{ds} ... dust scattering

Relative air mass:
simplest approximation: $m = 1/\cos Z$
better approximation (Kasten, 1966):

$$m = \frac{1}{\cos Z + 0.15 \times (93.885 - Z)^{-1.253}} \tag{4.1}$$

if $(m < 0)$, then $m = \infty$
$p_0 = 610$ on Mauna Kea summit

$$m' = m \times p_0/1013$$

Water vapor:
$w = 0.16$ cm for Mauna Kea according to `https://www.gemini.edu/observing/telescopes-and-sites/sites%23MKWV#MKWV` (assuming a typical $\tau(225\text{ GHz})$ of 0.08)

$$\begin{aligned}
\psi_{wa} &= 1 - 0.077(w\,m)^{0.30} \quad \text{McDonald (1960)} & (4.2)\\
\psi_{ws} &= 1 - 0.025\,w\,m & (4.3)
\end{aligned}$$

Rayleigh scattering: 8% at sea level according to Fig 3-3 in Bird and Hulstrom (1981)

$$\psi_{rs} = \exp(-0.08m') \qquad (4.4)$$

Aerosols: aerosol optical depth on Mauna Kea $= 0.0084 \times (\lambda/1\mu\text{m})^{-1.26}$ (Buton et al., 2013)

$$\begin{aligned}
\psi_{ds} &= \exp(-m \times 0.0084 \times 0.5^{-1.26}) & (4.5)\\
\psi_{da} &= \psi_{ds} \quad \text{assumes single scattering albedo of 0.5} & (4.6)
\end{aligned}$$

Direct sunlight:
$$I_0 = \psi_{wa}\psi_{da}\psi_{ws}\psi_{rs}\psi_{ds} \times (\text{solar constant})/R^2 \qquad (4.7)$$
(without the dimensional factors, this is the transmittance)

Diffuse sunlight:
$$D_0 = I_0 \cos(Z)\psi_{wa}\psi_{da}\frac{1 - \psi_{ws}\psi_{rs}\psi_{ds}}{2} \qquad (4.8)$$
Roundoff issue: if $(D_0 \leq 0)$, then $D_0 = 0$ because of -0.

Total short-wavelength flux:
$$F = I_0 \cos Z + D_0 \qquad (4.9)$$

Roundoff issue: if $(F \leq 0)$, then $F = 0$ because of -0.

Not included are the sensible heat flux and long-wave downward radiation.

Atmospheric contribution with terrain shadowing: If terrain irradiance is not included in the surface energy balance, it would be a disadvantage to reduce the diffuse sky irradiance due to obstruction by horizons, because that portion of the sky irradiance would need to be replaced by irradiance from land surfaces. If terrain irradiance is included, then see section 5.6 on how to evaluate the sky irradiance.

used in Schorghofer et al. (2017) and Schorghofer (2018)

Bibliography

Bird, R. E. and Hulstrom, R. L., 1981. A simplified clear sky model for direct and diffuse insolation on horizontal surfaces. Technical report, Golden, Colorado. Report No. SERI/TR-642-761.

Blanco-Muriel, M., Alarcón-Padilla, D. C., López-Moratalla, T., and Lara-Coira, M., 2001. Computing the solar vector. *Solar Energy* 70:431–441. doi: 10.1016/S0038-092X(00)00156-0.

Buton, C. et al., 2013. Atmospheric extinction properties above Mauna Kea from the Nearby SuperNova Factory spectro-photometric data set. *Astron. Astrophys.* 549:A8. doi: 10.1051/0004-6361/201219834.

Kasten, F., 1966. Albedo and sky radiance measurements in Greenland. *Arch. Meteor. Geophys. Bioklimatol.* B14:206–223. http://hdl.handle.net/11681/5813.

McDonald, J. E., 1960. Direct absorption of solar radiation by atmospheric water vapor. *Journal of Meteorology* 17:319–328. doi: 10.1175/1520-0469(1960)017%3C0319:DAOSRB%3E2.0.CO;2.

Nunez, M., 1980. The calculation of solar and net radiation in mountainous terrain. *Journal of Biogeography* 7:173–186. doi: 10.2307/2844709.

Schorghofer, N., 2018. Permafrost survey on the Maunakea summit plateau: Final report. Technical report, University of Hawaii. 28pp.

Schorghofer, N., Leopold, M., and Yoshikawa, K., 2017. State of high-altitude permafrost on tropical Maunakea volcano, Hawaii. *Permafrost and Periglacial Processes* 28:685–697. doi: 10.1002/ppp.1954.

Part 5

3D Surface Energy Balance

Energy Balance with Terrain Shadowing, Terrain Irradiance, and Sky Irradiance

History:
    2002–2005 Planar slopes (sec. 5.1 & 5.2)
    2010–2019 3D topography (sec. 5.3–5.7)

With 3-dimensional topography the surface energy balance is modified, compared to a horizontal unobstructed planar surface, for the following reasons:

DIRECT IRRADIANCE:
    1) changed incidence angle
    2) elevated horizons (terrain shadowing)

TERRAIN IRRADIANCE:
    3) reflected sunlight from visible land surfaces
    4) infrared emissions from visible land surfaces ("self-heating")

SKY IRRADIANCE (for bodies with atmospheres):
    5) restricted diffuse sky irradiance (short-wavelength and long-wavelength)

The incidence angle on a sloped surface is easily calculated. The elevated horizons change the time of sunset and sunrise, and also reduce the irradiance received from the atmosphere. Horizon determinations require that all other pixels in the domain are considered, and hence represent a non-local computational problem. Sunlight that is reflected from surfaces and the infrared emitted from the same surfaces are known as "terrain irradiance" and computed with the help of "view factors". Calculation of the terrain irradiance is computationally even more demanding than the horizons calculations.

5.1   Incidence Angle on Slope; Direct Solar Irradiance

The elevation β of the sun above a horizontal horizon is given in terms of geographic latitude λ, declination of the sun δ, and the hour angle h by

$$\sin \beta = \cos \lambda \cos \delta \cos h + \sin \lambda \sin \delta. \tag{5.1}$$

The angle θ of the sun above a sloped surface is

$$\sin \theta = \cos \alpha \sin \beta - \sin \alpha \cos \beta \cos(\Delta a), \tag{5.2}$$

where α is the slope angle and Δa is the difference between the azimuth of the sun and the azimuth of the topographic gradient. The sun is assumed to be below the horizon if either $\sin \beta < 0$ (horizontal horizon at infinity) or $\sin \theta < 0$ (self shadowing of slope). For 3D topography, a distant horizon, higher than the self shadowing slope, introduces an additional cutoff $e_{\max}$ (horizon elevation).

On an airless body the direct insolation is

$$Q_{\text{solar}} = \frac{S_0}{R^2}(1 - A) \sin \theta. \tag{5.3}$$

where S_0 is the solar constant, R the distance from the sun in AU, and A the albedo.

For Mars, the direct solar insolation is

$$Q_{\text{solar}} = \frac{S_0}{R^2}(1 - A)(1 - f)^{1/\max(\sin \beta, 0.04)} \sin \theta, \tag{5.4}$$

where f arises from the extinction in the atmosphere. This is a generalization of eq. (1.13) in subsection 1.2.4, where this expression is further justified.

5.2 Thermal Model for Tilted Planar Slope

Planar slopes are much simpler than the general 3D problem. This section describes a model for the thermal balance on a tilted plane, in the form of two coupled 1D thermal models, plus a 0D atmosphere. The model is for Mars, but easily simplified to airless bodies. It was used in Aharonson and Schorghofer (2006) and Schorghofer and Edgett (2006).

Let α denote the slope angle. The heat balance on the surface is

$$Q(\alpha) + k \left. \frac{\partial T}{\partial z} \right|_{z=0} = \epsilon \sigma T^4 + (\text{latent heat of CO}_2 \text{ frost}) \tag{5.5}$$

with

$$Q = Q_{\text{solar}}(\alpha) + Q_{\text{a,IR}}(\alpha) + Q_{\text{a,scat}}(\alpha) + Q_{\text{land}}(\alpha). \tag{5.6}$$

Q is the incoming radiation from the sun, atmosphere, and surfaces within field of view, T temperature, z the vertical coordinate, k the thermal conductivity, ϵ emissivity, and σ the Stefan-Boltzmann constant. The subscript a denotes contributions from the atmosphere. Figure 5.1 illustrates the contributions.

Terrain irradiance: The surface reemits radiation in all directions, but receives additional energy from surfaces in its field of view (terrain irradiance). This emission is weighted according to the incidence angle ι (Greek letter iota) and integrated over the spherical angle Ω subtended by the visible land surfaces. If we consider a horizontal surface at uniform temperature T_2 (Kreslavsky and Head, 2005):

$$Q_{\text{land}} = \epsilon_2 \sigma T_2^4 \int \cos \iota \, d\Omega = \sin^2 \left(\frac{\alpha}{2}\right) \epsilon_2 \sigma T_2^4. \tag{5.7}$$
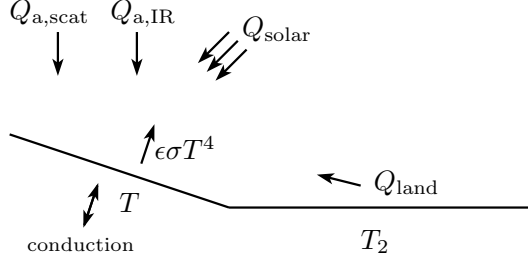
30

Figure 5.1: Contributions to the heat balance on a slope with surface temperature T.

If one assumes $T_2 = T$ and $\epsilon_2 = \epsilon$, then this term can be brought to the right-hand side of eq. (5.5), leading to an effective emissivity of $\epsilon \cos^2(\alpha/2)$. However, this is often not a good approximation, as demonstrated in Aharonson and Schorghofer (2006), Fig. 2b. It is more accurate to base T_2 on a separate 1D model for a flat surface.

Sky irradiance for planar slope. For bodies with atmosphere, the diffuse irradiance from the sky adds a small amount of energy to the surface.

For Mars, in the spirit of the Kieffer approximation (subsection 1.2.4),

$$Q_{a,IR} = \frac{S_0}{R^2} F_{sky} f_{IR} \sin \beta_{noon} \qquad \text{(all day)} \qquad (5.8)$$

and if the sun is up, then

$$Q_{a,scat} = \frac{S_0}{2R^2}(1 - A)F_{sky}f_{scat} \qquad \text{when } \sin \beta > 0 \qquad (5.9)$$

otherwise $Q_{a,scat} = 0$.

More than one definition of (sky) view factor F_{sky} and various approximations for the sky irradiance are used in the literature; see Flo Heggem et al. (2001) and Rakovec and Zakšek (2012). For isotropic (Lambertian) irradiance from the sky, the diffuse irradiance from the atmosphere is weighed by the cosine of the incidence angle. For a planar slope this results in $F_{sky} = \cos^2(\alpha/2)$.

Spiga and Forget (2008) have derived a more detailed parameterization for $Q_{a,scat}$ on a planar slope on Mars.

5.3   Horizons and Multigrids (Terrain Shadowing)

Shadowing by nearby topography (terrain shadowing) defines local horizons and is important for the energy balance. Horizons for each pixel are determined with azimuth rays, typically every 2° in azimuth, and the highest horizon in each direction is stored. For the purpose of horizon determination, the topography is represented by triangular facets. The horizon-finding calculation is implemented in `shadows.f90` and `shadow_subs.f90`.

The topography is defined on a rectangular coordinate grid with spatial resolution Δx in the longitude direction and Δy in the latitude direction. Curvature effects are not incorporated, i.e., the domain needs to be small compared to the radius of the body. Nor can the domain include the rotational pole. Surface normals are calculated using center-differences in x- and y-direction, and one-sided differences at the domain boundaries.

Multigrid Acceleration for Horizons Calculations: Use of spatial grids with various resolutions (multigrid method) dramatically accelerates the horizons calculation, because cells that are far from the point of interest are larger and fewer (Figure 5.2). For a domain with $N \times N$ pixels, the computational cost without multigrid method is $O(N^4)$. With multigrid, it is $O(N^2 \log N)$. In the current implementation of the multigrid method, up to ten grids can be used; the difference in resolution between the coarsest and finest grids is a factor of 2^{10-1}. If the multigrid method is not used, an optional cut-off radius `RMAX` can be introduced, so spatial distances larger than `RMAX` are ignored.
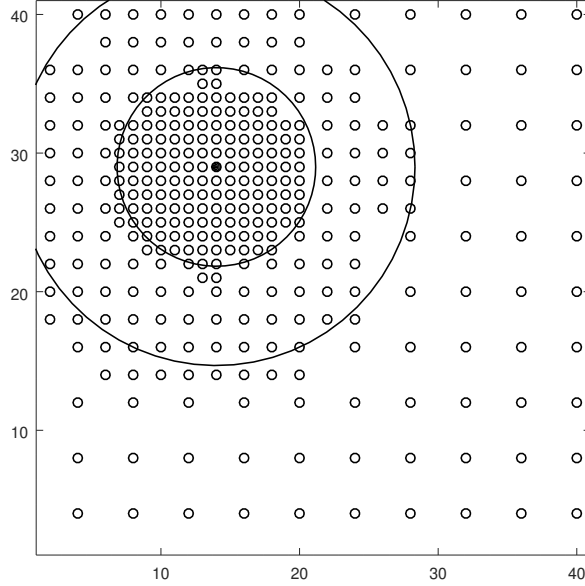
Figure 5.2: Example of multigrid (empty dots) used to determine horizons for one point of interest (solid dot). A progressively downsampled topography is used as the distance from the point of interest increases. This example uses three levels of grids.

First, grids of various resolutions are created, until the coarsest grid consists of only a few pixels along the narrower side of the rectangular domain. Grid coordinates of the coarse cells are also grid coordinates on the finest grid. Progressive downsampling by factors of two involves weighted averaging among the 8 nearest neighbors and the center point itself, such that $\int \int h(x, y) dx dy$ is conserved (other than at the edges of the domain).

The determination of the grid points to be used for each point of interest begins by looping through the coarsest grids. If the distance of the center point to the point of interest is too small, the algorithm proceeds by looping through the four finer cells that make up the coarse cell. This is done recursively, until the resolution is appropriate for the distance or the finest grid is reached. This results in multigrids as in Figure 5.2.

5.4 Governing Equations with Terrain Irradiance

The equation governing the energy balance on the surface on an airless body is

$$(1 - A)(Q_{\text{direct}} + Q_{\text{refl}}) + k\frac{\partial T}{\partial z} + \epsilon Q_{\text{IR}} = \epsilon\sigma T^4 \tag{5.10}$$

where A is albedo, Q_{direct} incoming solar radiation (insolation), k thermal conductivity, T temperature, z depth below surface, ϵ emissivity, and σ the Stefan-Boltzmann constant. The flux Q_{direct} is determined from the declination of the Sun, latitude, and hour angle, eqs. (5.1, 5.2). Due to topography, reflected sunlight (Q_{refl}) and thermal emission (Q_{IR}) from other surfaces need to be added.

The diffuse terrain irradiance depends on the spherical angle $d\Omega$ subtended by the facet, and similarly for infrared emission:

$$Q_{\text{refl}}(x, y) = \frac{1}{\pi} \iint A' \left[Q'_{\text{direct}} + Q'_{\text{refl}}\right] \cos\iota \, d\Omega(x, y, x', y') \tag{5.11}$$

$$Q_{\text{IR}}(x, y) = \frac{1}{\pi} \iint \left[\epsilon\sigma T'^4 + (1 - \epsilon)Q'_{\text{IR}}\right] \cos\iota \, d\Omega(x, y, x', y') \tag{5.12}$$

where primed variables are evaluated at (x', y') and unprimed variables at (x, y). The integrals are over all facets within the field of view, and ι is the angle between the surface normal and the line of sight that connects the two facets. The term with the factor $(1 - \epsilon)$ is reflected infrared.

In the literature these equations are often written in terms of a "view factor"

$$V_{ij} = \frac{\cos\iota_i \cos\iota_j}{\pi r_{ij}^2} d\mathcal{A}_j \tag{5.13}$$

where r_{ij} is the distance between the two facets, $\iota_i = \iota(x, y)$, $\iota_j = \iota(x', y')$, and $d\mathcal{A}$ the differential surface area. Since

$$d\Omega = \frac{\cos\iota_j}{r_{ij}^2} d\mathcal{A}_j$$

this is equivalent. The discretized equations then take the form

$$Q_{\text{refl}\,i} = \sum_{j'} A_{j'} \left[Q_{\text{direct}\,j'} + Q_{\text{refl}\,j'}\right] V_{i,j'} \tag{5.14}$$

$$Q_{\text{IR}\,i} = \sum_{j'} \left[\epsilon\sigma T_{j'}^4 + (1 - \epsilon)Q_{\text{IR},j'}\right] V_{i,j'} \tag{5.15}$$

Equations (5.11) and (5.12) are linear equations for Q_{refl} and Q_{IR}, widely known as radiosity equations. However, for a time-dependent problem with subsurface heat conduction, it is not necessary to solve the radiosity equations. Instead, these equations can be used as explicit time-stepping procedure with Q_{refl}, T, and Q_{IR} on the right hand side evaluated at the previous time step n, whereas Q_{direct} and A can be evaluated at time step $n + 1$.

5.5 View Factors

Mutual visibility is determined by calculating the slope of the line that connects the two surface facets and comparing it to the maximum topographic slope along a ray in the same direction, tracing outward. (Hence there is a sort involved that is not necessary if only horizons are needed.)

Ultimately, the view factor of all mutually visible facets is calculated and stored. For the purpose of view factors, the topography is represented by rectangles. The visibility and view factor calculations are implemented in `fieldofviews.f90` and `fieldofview_subs.f90`.

View factor values can be validated for a bowl-shaped crater (a spherical cap). Inside a sphere of radius R

$$\frac{\cos \iota_i \cos \iota_j}{r_{ij}^2} = \frac{\cos^2 \iota}{(2R \cos \iota)^2} = \frac{1}{4R^2} \tag{5.16}$$

for any pair of facets i, j. The viewfactor (5.13) is therefore $V_{ij} = d\mathcal{A}_j/(4\pi R^2)$.

The differential solid angle can be written as

$$d\Omega = \cos e \, de \, d\varphi \tag{5.17}$$

where φ is azimuth and e the elevation (an angle) above the horizon. The solid angle of the entire landscape within field of view is

$$\Omega_{\text{land}} = \iint d\Omega = \int_0^{2\pi} \int_0^{e(\varphi)} de \, d\varphi \cos e = \int_0^{2\pi} d\varphi \, \sin(e(\varphi)) \tag{5.18}$$

The spherical angle of the visible sky is $\Omega_{\text{sky}} = 2\pi - \Omega_{\text{land}}$. It is also helpful to introduce the abbreviation

$$G = \frac{1}{\pi} \iint \cos \iota \, d\Omega \tag{5.19}$$

For a half-sphere $G = 1$.

Next several special cases, with increasing complexity, are considered:

a) In the special case of a surface covered by a dome at uniform temperature,

$$\iint \cos \iota \, d\Omega = \int_0^{2\pi} d\varphi \int_0^{\pi/2} de \sin e \cos e = 2\pi \int_0^{\pi/2} de \sin e \cos e = 2\pi \frac{1}{2} \sin^2(\pi/2) = \pi$$

Hence $G = 1$ and (5.12) becomes $Q_{\text{IR}} = \epsilon \sigma T'^4$ (plus the reflected infrared, but the emissivity of the sky is different from the emissivity of the surface).

b) Planar slope with a single temperature combined with a horizontal surface with another temperature, as in Figure 5.1. In this case, $\Omega = 2\alpha$, so that at $\alpha = \pi/2$ a quarter of the sphere remains. For the slope, the horizon height $e(\varphi)$ along direction φ is related by $\tan \alpha \cos \varphi = \tan e$.

For integration practice,

$$\begin{aligned} \iint d\Omega &= \int_{-\pi/2}^{\pi/2} d\varphi \int_0^{e(\varphi)} de \cos e = \int_{-\pi/2}^{\pi/2} d\varphi \sin(e(\varphi)) \\ &= \int_{-\pi/2}^{\pi/2} d\varphi \frac{\tan \alpha \cos \varphi}{\sqrt{1 + \tan^2 \alpha \cos^2 \varphi}} = 2\alpha \end{aligned}$$

34

where $\sin e = \tan e / \sqrt{1 + \tan^2 e}$ was used. The integral of interest

$$
\begin{aligned}
\iint \cos\iota \, d\Omega &= \int_{-\pi/2}^{\pi/2} d\varphi \int_0^{e(\varphi)} de \sin e \cos e \\
&= \int_{-\pi/2}^{\pi/2} d\varphi \frac{1}{2} \sin^2(e(\varphi)) = \frac{1}{2} \int_{-\pi/2}^{\pi/2} d\varphi \frac{\tan^2\alpha \cos^2\varphi}{1 + \tan^2\alpha \cos^2\varphi} \\
&= \frac{\pi}{2}(1 - \cos\alpha) = \pi \sin^2\left(\frac{\alpha}{2}\right)
\end{aligned}
$$

In this case, $G = \sin^2(\alpha/2)$ and (5.12) becomes

$$
Q_{\mathrm{IR}} = \epsilon\sigma T'^4 \sin^2\left(\frac{\alpha}{2}\right) \tag{5.20}
$$

plus the reflected infrared, which reproduces (5.7).

c) Uniform temperature, locally flat:

$$
\iint \cos\iota \, d\Omega = \int_0^{2\pi} \int_0^{e(\varphi)} de \, d\varphi \cos e \sin e = \frac{1}{2} \int_0^{2\pi} d\varphi \sin^2(e(\varphi))
$$

G equals $\sin^2 e(\varphi)$ averaged over azimuths. For small e, $G \ll \Omega_{\mathrm{land}}/(2\pi)$.

d) Uniform temperature, not locally flat:

$$
\sin\theta = \cos\iota = \cos\alpha \sin\beta + \sin\alpha \cos\beta \cos(\Delta a)
$$

where α is the local slope angle. There is now also a lower limit on the elevation angle, $e_{\min}(\varphi)$, from the self-shadowing of the slope, so $\sin\theta$ will never become negative, and therefore

$$
\tan e_{\min} = -\tan\alpha \cos(\Delta a)
$$

which can be positive or negative.

The integral of interest is

$$
\iint \cos\iota \, d\Omega = \int_0^{2\pi} \int_{e_{\min}(\varphi)}^{e(\varphi)} de \, d\varphi \cos e \left[\cos\alpha \sin e + \sin\alpha \cos e \cos(\Delta a)\right] \tag{5.21}
$$

and the integrals over e can be computed as

$$
\begin{aligned}
\frac{1}{\pi} \int de \cos e \sin e &= \frac{1}{2\pi} \sin^2 e \\
\frac{1}{\pi} \int de \cos^2 e &= \frac{1}{2\pi}(e + \sin e \cos e)
\end{aligned}
$$

G can be pre-computed from static geometric information:

$$
\begin{aligned}
G &= \frac{\cos\alpha}{2\pi} \int_0^{2\pi} d\varphi \left(\sin^2 e - \sin^2 e_{\min}\right) + \\
&\quad + \frac{\sin\alpha}{2\pi} \int_0^{2\pi} d\varphi \, \cos(\Delta a)(e + \sin e \cos e - e_{\min} - \sin e_{\min} \cos e_{\min}) \tag{5.22}
\end{aligned}
$$

An approximation for small e is

$$G \approx \frac{\sin\alpha}{\pi} \int_0^{2\pi} d\varphi \, \cos(\Delta a)(\sin e - \sin e_{\min})$$

For comparison, the surface area (in steradian) visible from an inclined surface is

$$\Omega_{\text{land}} = \iint d\Omega = \int_0^{2\pi} \int_{e_{\min}(\varphi)}^{e(\varphi)} de \, d\varphi \, \cos e = \int_0^{2\pi} d\varphi \, (\sin e - \sin e_{\min}) \qquad (5.23)$$

Equations (5.12) and (5.22) invite a particularly useful approximation for the terrain irradiance. Assuming all land within field of view has the same surface temperature, Q_{IR} can be calculated from G and view factors for individual facets are not required. One choice for the uniform temperature is the (time-dependent) surface temperature of a horizontal and unobstructed surface. Similarly, Q_{refl} can be calculated the same way when assuming AQ_{direct} is uniform on land within the field of view. After horizons and G have been calculated, the surface energy balance calculations for each pixel are independent of one another, and the entire model implementation can be easily parallelized.

5.6   Diffuse Sky Irradiance in the Presence of Horizons

In the literature more than one definition of (sky) view factor F_{sky} and various approximations for the sky irradiance are in use; see Flo Heggem et al. (2001) and Rakovec and Zakšek (2012). The geometric factor F_{sky} defines what fraction of the sky irradiance for an unobstacted location ($F_{\text{sky}} = 1$) still arrives at a location obstructed by terrain.

One option is to assume the energy contribution is proportional to the spherical angle of the visible sky. In this case, F_{sky} is the spherical angle of the visible sky divided by 2π, which can be calculated from either the horizon heights or the sum of view factors of the landscape segments. For a planar slope tilted by an angle α, $F_{\text{sky}} = 1 - \alpha/2\pi$.

The alternative is to weigh the diffuse irradiance from the atmosphere with the cosine of the incidence angle. This is the view factor V as defined above for land segments. This corresponds to isotropic (Lambertian) radiation from the sky. The factor F_{sky} then becomes identical to G_{sky}. For computing the sky view factor, eq. (5.22) can be used with $e_{\min}$ replaced by e, and e replaced by $\pi/2$:

$$G_{\text{sky}} = \frac{\cos\alpha}{2\pi} \int_0^{2\pi} d\varphi \, (1 - \sin^2 e) + \frac{\sin\alpha}{2\pi} \int_0^{2\pi} d\varphi \, \cos(\Delta a) \left(\frac{\pi}{2} - e - \sin e \cos e\right) \quad (5.24)$$

$$= \frac{\cos\alpha}{2\pi} \int_0^{2\pi} d\varphi \, \cos^2 e - \frac{\sin\alpha}{2\pi} \int_0^{2\pi} d\varphi \, \cos(\Delta a) \, (e + \sin e \cos e) \qquad (5.25)$$

This equation can be found in Dozier and Frew (1990). For a planar slope $G_{\text{sky}} = \cos^2(\alpha/2)$.

For Mars, in the spirit of the Kieffer approximation (subsection 1.2.4),

$$Q_{\text{a,IR}} = \frac{S_0}{R^2} F_{\text{sky}} f_{\text{IR}} \sin\beta_{\text{noon}} \qquad \text{(all day)} \qquad (5.26)$$

and if the sun is up, then

$$Q_{\text{a,scat}} = \frac{S_0}{2R^2}(1-A)F_{\text{sky}}f_{\text{scat}} \qquad \text{when } \sin\beta > 0 \tag{5.27}$$

otherwise $Q_{\text{a,scat}} = 0$.

For terrestrial applications, other expressions may be available to quantify the sky irradiance. For example, section 4.1 provides a formula for the diffuse short-wave clear-sky irradiance on Mauna Kea. Such formulas for flat unobstracted terrain can be adopted for obstructed topography using a geometric factor F_{sky}.

5.7 Outline of Implementation

The calculations are separated into two parts.

The first, described in section 5.3, determines the horizons for all pixels and (optionally) view factors of all facets with all other facets. This information is written to files `horizons.dat` and `viewfactors.dat`, respectively. This part is easily parallelized, as calculations for each pixel are independent of one another although the entire topography has to be loaded into memory at once. For parallelization, one slice of the spatial domain is run on each CPU thread. It can be submitted to a computer cluster as an array job.

In the `horizons` file, each line is preceded by the integer pixel coordinates. The file is rectangular, and the number of entries is (number of azimuth rays + 2)×(number of topographic pixels). The `viewfactors` file is giant and it is not rectangular. Each line in the output file corresponds to a topographic pixel and at the beginning specifies the number of pixels within field of view. Each visible pixel has then three numbers stored with it: The two integer pixel coordinates and the view factor, V_{ij}, for this pixel. Non-visible pixels are not stored.

Horizons calculations are implemented in `shadows.f90` and its subroutines. If the view factors are desired, use `fieldofviews.f90`. Horizon heights are also calculated within `fieldofviews.f90`, but with a slightly different algorithm than in `shadows.f90`.

The second part simulates the time evolution of illumination and surface temperature as the sun moves through the sky, using the horizons and (optionally) the field of view as input. The horizons are read in a module called `newhorizons`, which also interpolates horizon elevations for any desired azimuth. The field of view information is read with a separate subroutine. To save memory, the pixel coordinates are stored as 2-byte integers and the view factors as 4-byte floating point numbers, respectively, half of the common byte lengths.

The surface energy balance is integrated over time at steps of a fraction (e.g., 1/50th) of a solar day. Surface temperature and illumination are updated at every time step. The names of the main programs start with `cratersQ_*` (Table 5.1).

The current implementations use the following naming convention. The input topography to `horizons.f90` is *name*.`xyz`, and the output will be `horizons.dat` for the sequential implementation or `horizon.`*arg* for the parallel implementation, where *arg* is an integer. `cratersQ_*` expects input files *name*.`xyz`, `horizons.`*name*, and optionally `viewfactors.`*name*. File names and their associated parameters are specified in module `filemanager`, that the user edits.

Table 5.1: Overview of current implementations

Main program	Task	Reflections	Parallel
shadows	pre-calculate horizons, optional multigrid	N/A	yes
fieldofviews	pre-calculate view factors, no multigrid	N/A	yes
insol3d_earth	direct insolation only, Mauna Kea atm.	no	no
insol3d_mars	direct insolation only, no atmosphere	no	no
cratersQ_equilbr	equilibrium solution for airless body	yes	no
cratersQ_moon	airless body	yes	no
cratersQ_mars	Mars orbit and atmosphere	G-approx.	no
cratersQ_mars_parallel	Mars orbit and atmosphere	G-approx.	yes
cratersQ_mars_full	Mars orbit and atmosphere	yes	no

The model also includes 1D subsurface heat conduction, eq. (1.1). Subsurface temperatures need to be equilibrated, and hence the entire model needs to be run much longer than would be necessary without subsurface heat. Lateral subsurface heat conduction is neglected. Without subsurface conduction, equilibrium temperatures, according to eq. (5.10) with $k = 0$, can be used, and in this case only a few steps of equilibration are needed to account for several orders of reflection.

insol3d_earth was used in Schorghofer et al. (2017) and Schorghofer (2018), cratersQ_mars_parallel in Schorghofer et al. (2019), cratersQ_moon in Hayne et al. (2021), and cratersQ_mars_full in Schorghofer (2020).

Bibliography

Aharonson, O. and Schorghofer, N., 2006. Subsurface ice on Mars with rough topography. *J. Geophys. Res.* 111(E11):E11007. doi: 10.1029/2005JE002636.

Dozier, J. and Frew, J., 1990. Rapid calculation of terrain parameters for radiation modeling from digital elevation data. *IEEE Transactions on Geoscience and Remote Sensing* 28(5): 963–969. doi: 10.1109/36.58986.

Flo Heggem, E. S., Etzelmüller, B., and Berthling, I., 2001. Topographic radiation balance models: sensitivity and application in periglacial geomorphology. *Norsk Geografisk Tidsskrift-Norwegian Journal of Geography* 55(4):203–211. doi: 10.1080/00291950152746531.

Hayne, P. O., Aharonson, O., and Schorghofer, N., 2021. Micro cold traps on the Moon. *Nature Astronomy* 5:169–175. doi: 10.1038/s41550-020-1198-9.

Kreslavsky, M. A. and Head, J. W., 2005. Mars at very low obliquity: atmospheric collapse and the fate of volatiles. *Geophys. Res. Lett.* 32(12):L12202. doi: 10.1029/2005GL022645.

Rakovec, J. and Zakšek, K., 2012. On the proper analytical expression for the sky-view factor and the diffuse irradiation of a slope for an isotropic sky. *Renewable Energy* 37(1): 440–444. doi: 10.1016/j.renene.2011.06.042.

Schorghofer, N., 2018. Permafrost survey on the Maunakea summit plateau: Final report. Technical report, University of Hawaii. 28pp.

Schorghofer, N., 2020. Mars: Quantitative evaluation of crocus melting behind boulders. *Astrophys. J.* 890:49. doi: 10.3847/1538-4357/ab612f.

Schorghofer, N. and Edgett, K. S., 2006. Seasonal surface frost at low latitudes on Mars. *Icarus* 180(2):321–334. doi: 10.1016/j.icarus.2005.08.022.

Schorghofer, N., Leopold, M., and Yoshikawa, K., 2017. State of high-altitude permafrost on tropical Maunakea volcano, Hawaii. *Permafrost and Periglacial Processes* 28:685–697. doi: 10.1002/ppp.1954.

Schorghofer, N., Levy, J. S., and Goudge, T. A., 2019. High-resolution thermal environment of recurring slope lineae in Palikir Crater, Mars, and its implications for volatiles. *J. Geophys. Res.* 124:2852–2862. doi: 10.1029/2019JE006083.

Spiga, A. and Forget, F., 2008. Fast and accurate estimation of solar irradiance on martian slopes. *Geophys. Res. Lett.* 35:L15201. doi: 10.1029/2008GL034956.

Part 6

Surface-bounded Exospheres

Monte-Carlo Model of Ballistically Hopping Molecules in Gravitationally-Bound Exospheres

History: developed 2012–2017
Core routines are implemented in `montecarlo.f90`

6.1   Introduction

The ballistic trajectories of neutral molecules or atoms in a surface-bounded exosphere are simulated with a Monte-Carlo method. Individual water molecules are launched with probabilistically distributed cartesian velocity components that amount to a random initial azimuth and thermal speed appropriate for the local surface temperature. The model then computes the molecule's impact location and time analytically. An event-driven algorithm is used, where landing and launching events are processed in time-order. Events are scheduled and processed until the molecule is destroyed or lost or until its landing or launch time is beyond the next thermal model time step, when surface temperatures are updated.

   Each molecule has a longitude $\mathtt{p_r}[1]$, latitude $\mathtt{p_r}[2]$, status $\mathtt{p_s}$ (on surface =0, in-flight =1, lost or cold-trapped < 0), and time to the next event $\mathtt{p_t}$ (until it arrives on the surface or until it will leave the surface). Negative status values can be used to keep track of where the particle is trapped or how it was lost. Surface temperatures are calculated with a 1D thermal model, as in Part 1.

6.2   Ballistic Flight on Sphere

d ... flight distance (measured along surface of sphere)
t ... duration of flight
τ_{res} ... surface residence time
τ_{dissoc} ... photo-destruction time scale
v_{esc} ... escape speed
v_1 ... initial velocity along longitude direction
v_2 ... initial velocity along meridian
v_3 ... initial vertical (radial) velocity component
az ... azimuth

$\Delta\phi$ ... difference in longitude
λ ... latitude
M ... molar mass
R_{moon} ... radius of body

A ballistic molecule moves on a plane that goes through the center of sphere/body; the ground track is thus part of a great circle.

6.2.1   Constant gravity

For constant g,

$$t \;=\; 2v_3/g \tag{6.1}$$

$$d \;=\; \frac{2}{g}v_3\sqrt{v_1^2 + v_2^2} \tag{6.2}$$

If $|v| > 0.4v_{\text{esc}}$, then use non-uniform gravity formulae (Sec. 6.2.2)
If $|v| > v_{\text{esc}}$, then gravitational escape
    The landing latitude and longitude $(\lambda_2, \phi_1 + \Delta\phi)$ are calculated from the starting coordinates (λ_1, ϕ_1) with the following equations:

$$\cos(az) \;=\; v_2/\sqrt{v_1^2 + v_2^2} \tag{6.3}$$

$$\sin\lambda_2 \;=\; \sin(d/R_{\text{moon}})\cos(\lambda_1)\cos(az) + \sin(\lambda_1)\cos(d/R_{\text{moon}}) \tag{6.4}$$

$$\cos\lambda_2 \;=\; \sqrt{1 - \sin^2\lambda_2} \tag{6.5}$$

$$\cos(\Delta\phi) \;=\; \frac{\cos(d/R_{\text{moon}})\cos(\lambda_1) - \sin(\lambda_1)\sin(d/R_{\text{moon}})\cos(az)}{\cos\lambda_2} \tag{6.6}$$

Roundoff issues: if $\cos(\Delta\phi) > +1$ then $\cos(\Delta\phi) = +1$; if $\cos(\Delta\phi) < -1$ then $\cos(\Delta\phi) = -1$.

$p_r(2) = \arcsin(\sin\lambda_2)$
$\Delta\phi = \arccos(\cos(\Delta\phi))$ for normalization
if $v_1 < 0$, then $\Delta\phi = -\Delta\phi$
$p_r(1) = p_r(1) + \Delta\phi$
if $(\cos\lambda_2 == 0)$ then on pole
$p_r(1)$ is normalized to 0...360°.

$p_t = p_t + t$

6.2.2   Non-uniform gravity

Ballistic travel distance d and flight duration t can also be calculated analytically for a radially dependent gravitational acceleration. Radial variations in g are small for typical thermal speeds on Mercury and on the Moon, but necessary for Ceres and for super-thermal species on the Moon. The following equations are derived from those in Vogel (1966) and Kegerreis et al. (2017).

a ... semi-major axis of ballistic trajectory

e ... eccentricity of ballistic trajectory

α ... zenith angle of launch velocity, $\alpha = \arctan\left(\sqrt{v_1^2 + v_2^2}/v_3\right)$

Instead of (6.1) and (6.2) use

$$\gamma = \left(|v|/v_{\text{esc}}\right)^2 \tag{6.7}$$

$$a = \frac{R_{\text{moon}}}{2(1-\gamma)} \tag{6.8}$$

$$e = \sqrt{1 - 4\gamma(1-\gamma)\sin^2\alpha} \tag{6.9}$$

$$d = 2R_{\text{moon}}\arccos\left(\frac{1}{e}(1 - 2\gamma\sin^2\alpha)\right) \tag{6.10}$$

$$E_p = 2\arctan\left(\sqrt{\frac{1+e}{1-e}}\tan\frac{d}{4R_{\text{moon}}}\right) \tag{6.11}$$

$$t = \frac{R_{\text{moon}}}{v_{\text{esc}}}\frac{E_p + e\sin E_p}{(1-\gamma)^{3/2}} \tag{6.12}$$

These equations are not suitable for small launch velocities due to roundoff.

Roundoff issues:

a) If e is very close to 1 (fast near-horizontal launch), then based on Taylor expansion of (6.10) and (6.11),

$$d = 4\gamma R_{\text{moon}}\sin\alpha \tag{6.13}$$

$$E_p = 2\arctan\sqrt{\frac{\gamma}{1-\gamma}} \tag{6.14}$$

b) If $1 - 2\gamma\sin^2\alpha > e$ (horizontal launch), do something, otherwise $d = \texttt{NaN}$

Then use (6.3)–(6.6) as before.

6.2.3   Coriolis effect

The Coriolis effect is incorporated by adding tangential velocities but subtracting the distance the surface has traveled during time of flight.

At launch:
$$v_1 = v_1 - \frac{2\pi R_{\text{moon}}}{\text{siderealDay}}\cos(p_r(2)) \tag{6.15}$$

After landing:
$$p_r(1) = p_r(1) + t/\text{siderealDay} \tag{6.16}$$

The Coriolis effect is negligible on the Moon and on Mercury, but noticeable on Ceres.

	M	τ_{dissoc} (s)	
H_2O	18.015	20×3600	Potter and del Duca (1964)
H_2O		1/12.6e-6	Crovisier (1989), normal sun
H_2O		1/23.0e-6	Crovisier (1989), active sun
He	4.0026	1.9e7	Killen and Ip (1999)
Ar-40	39.96	3.2e6	Killen and Ip (1999)

Table 6.1: Some pertinent parameters. τ_{dissoc} = photodissociation time scale at 1 AU

6.3 Other Model Components

6.3.1 Initial velocities

At launch, each of the three velocity components is picked from a probability distribution. For a Maxwellian distribution, each velocity component is picked from a Gaussian distribution with standard deviation $\sqrt{T_{surf}8314.5/M}$. This also results in uniformly distributed launch azimuths. Other probability distributions can be implemented, if desired. An Armand (also known as Maxwell-Boltzmann-Flux) distribution is provided as an option in the code.

6.3.2 Photo-destruction

Molecules are lost in-flight by photo-destruction (Table 6.1), at a rate of $t/(\tau_{dissoc}R^2)$, where R is the distance from the sun, often approximated by the semi-major axis. Requires incident flux $Q > 0$, since this only occurs on the dayside. A comprehensive compilation of photo-destruction rates can be found in Huebner et al. (1992). A database is maintained at http://phidrates.space.swri.edu/.

6.3.3 Event driver

Process events over the time step of the thermal model Δt_T, e.g., one hour

```
if (p_t > Δt_T) exit
case(p_s < 0) exit !  not alive
case(p_s==0) !  leaving
   hop once, update p_t
case(p_s==1) !  landing
   if (incoldtrap) then
      p_t = ∞
      cycle
   endif
   evaluate τ_res(T_surf)
   p_t = p_t + τ_res
```

After all events within Δt_T are processed, subtract Δt_T from all times: if ($\mathtt{p_s}$ >= 0) $p_t = p_t - \Delta t_T$. (Moving time zero helps avoid truncation errors after a long run.)

6.3.4   Residence times

Temperature also sets the residence time of water molecules on the surface, which is negligible on most of the lunar dayside and very long on most of the lunar nightside. Many older models use a binary choice, where molecules either immediately hop on the day side or reside indefinitely on the surface on the nightside. This model uses a molecular residence time that depends continuously on temperature instead of a threshold temperature.

For crystalline ice, the average molecular surface residence time only depends on temperature T, but for adsorbed water it is also a function of the adsorbate density θ (number of H_2O molecules per area). The average residence time is given by

$$\tau_{\text{res}} = \frac{\theta_m}{E(T,\theta)} \tag{6.17}$$

where E is the sublimation rate and $\theta_m = 10^{19}$ m^{-2} is the areal number density of an H_2O monolayer. A special case of this parametrization is $\tau_{\text{res}} = c\theta_m/E(T)$, where E is the sublimation rate of pure ice. For pure ice $c = 1$. For example, $c = 1/400$ is reasonable for 0.1 monolayers (Schorghofer and Aharonson, 2014). The functional form of $E(T)$ is almost the same as using a vibrational frequency multiplied by a Boltzmann (Arrhenius) factor.

For non-condensible exospheric species, e.g., helium, $\tau_{\text{res}} = 0$.

Discussion: A fraction of particles bounces elastically from the surface rather than accommodating thermally and leaving at a velocity unrelated to the incoming velocity. The fraction is closely related to the "accommodation coefficient" or "condensation coefficient", and it is temperature dependent. The equilibrium vapor pressure is defined as the flux of water molecules from the gas to the condensed phase being equal to the flux in the opposite direction. Elastic (non-condensing) bounces are not directly implemented in the model.

The exosphere model was used in Schorghofer (2014) (with constant g) and Schorghofer et al. (2016, 2017a,b) (with non-uniform gravity).

Bibliography

Crovisier, J., 1989. The photodissociation of water in cometary atmospheres. *Astron. Astrophys.* 213:459–464.

Huebner, W. F., Keady, J. J., and Lyon, S. P., 1992. Solar photo rates for planetary atmospheres and atmospheric pollutants. *Astrophysics and Space Science* 195:1–294. doi: 10.1007/978-94-017-3023-5_1.

Kegerreis, J. A., Eke, V. R., Massey, R. J., Beaumont, S. K., Elphic, R. C., and Teodoro, L. F., 2017. Evidence for a localized source of the argon in the lunar exosphere. *J. Geophys. Res.* 122:2163–2181. doi: 10.1002/2017JE005352.

Killen, R. M. and Ip, W.-H., 1999. The surface-bounded atmospheres of Mercury and the Moon. *Reviews of Geophysics* 37:361–406. doi: 10.1029/1999RG900001.

Potter, A. E. and del Duca, B., 1964. Lifetime in space of possible parent molecules of cometary radicals. *Icarus* 3:103. doi: 10.1016/0019-1035(64)90051-X.

Schorghofer, N., 2014. Migration calculations for water in the exosphere of the Moon: Dusk-dawn asymmetry, heterogeneous trapping, and D/H fractionation. *Geophys. Res. Lett.* 41: 4888–4893. doi: 10.1002/2014GL060820.

Schorghofer, N. and Aharonson, O., 2014. The lunar thermal ice pump. *Astrophys. J.* 788: 169. doi: 10.1088/0004-637X/788/2/169.

Schorghofer, N., Mazarico, E., Platz, T., Preusker, F., Schröder, S., Raymond, C., and Russell, C., 2016. The permanently shadowed regions of dwarf planet Ceres. *Geophys. Res. Lett.* 43:6783–6789. doi: 10.1002/2016GL069368.

Schorghofer, N., Byrne, S., Landis, M. E., Mazarico, E., Prettyman, T. H., Schmidt, B. E., Villarreal, M. N., Castillo-Rogez, J., Raymond, C. A., and Russell, C. T., 2017a. The putative cerean exosphere. *Astrophys. J.* 850:85. doi: 10.3847/1538-4357/aa932f.

Schorghofer, N., Lucey, P., and Williams, J.-P., 2017b. Theoretical time variability of mobile water on the moon and its geographic pattern. *Icarus* 298:111–116. doi: 10.1016/j.icarus.2017.01.029.

Vogel, U., 1966. Molecular fluxes in the lunar atmosphere. *Planetary and Space Science* 14: 1233–1252. doi: 10.1016/0032-0633(66)90078-X.